~~Wildfire-atmosphere interactions during~~ The impact of the Santa Coloma de Queralt fire on the atmospheric boundary layer: the development of a fire-induced circulation

Tristan Roelofs[1], Marc Castellnou[1,2], Jordi Vilà-Guerau de Arellano[1], Martin Janssens[1], and Chiel van Heerwaarden[1]

[1]Meteorology and Air Quality Group, Wageningen University & Research, The Netherlands
[2]Catalan Fire & Rescue Service, Bombers GRAF, Barcelona, Spain

Correspondence: Tristan Roelofs (Tristan.roelofs@wur.nl)

Abstract. High fireline intensities during extreme wildfire events can trigger pyro-convection, causing unpredictable fire spread behaviour, including faster-than-predicted fire spread and continued burning throughout the night. ~~Earlier studies hypothesised that the main~~ Previous studies showed that pyro-convection modifies the surrounding wind patterns. We hypothesised that fire-modified winds would cause heating and drying at the surface by transporting relatively warm, dry air towards the surface, thereby providing a potential explanation for nighttime burning. To investigate the impact of pyro-convection on the ~~fire behaviour is through the acceleration of the rear inflow. To assess this hypothesis~~atmosphere, we used MicroHH to create a high-resolution (25 m) turbulence-resolving 3D large-eddy simulation (25.6 by 38.4 km^2) of the Santa Coloma de Queralt fire ~~. We validated~~ (Catalonia, Spain, July 24, 2021). We evaluated the in-plume virtual potential temperature using ~~sounding~~ radiosonde measurements, to our knowledge, a novel approach for ~~validating~~ evaluating large-eddy simulations of pyro-convection. In-depth analysis of ~~the~~ wind patterns revealed an increase in rear inflow due to pyro-convection~~, as well as a frontal inflow of comparable magnitude, as part of~~. Additionally, the simulation revealed the development of a fire-induced circulation ahead of the fire~~. The frontal inflow could counteract the accelerated rear inflow and is associated with fire-generated vortices and long-range spotting. Additionally, we found~~, located between the convective plume and downdrafts 2 km ahead of the fire. We showed that the fire-induced circulation simultaneously deepens and lowers the boundary layer in the 4 km ahead~~, thereby disrupting the transition from the convective daytime to a stably stratified nighttime boundary layer. This disruption provides a plausible explanation for the sustained nighttime burning during the Santa Coloma de Queralt fire. Therefore, we argue that the primary impact of pyro-convection on wildfire behaviour depends on the balance between wind patterns at the rear and in front of the fire (revised hypothesis), rather than solely on the acceleration of the rear inflow (original hypothesis~~. Hence, we reject the original hypothesis that fire-modified winds cause surface heating and cooling. Instead, we found that the fire-modified winds, specifically the fire-induced circulation, altered the thermodynamic structure of the atmospheric boundary layer at higher altitudes (> 0.25 km).

1 Introduction

Extreme wildfire events ~~occur when the fire line intensity of wildfires exceeds~~ are defined by fire behaviour that surpasses the extinguishing capacity of ~~the fire service of~~ fire services, indicated by factors such as high rates of spread, erratic spotting, or fireline intensities exceeding 10 MW m^{-1} (Tedim et al., 2018). During ~~these events~~ events with such intensity, the high ~~fire line~~ fireline intensity can trigger significant upward convective motions (i.e. pyro-convection), which affect the wind speed and direction in the direct surroundings of the wildfire. The altered winds will change the fire behaviour (Sun et al., 2009), impacting the ~~fire line~~ fireline intensity and, subsequently, feed back on the pyro-convection. This feedback loop is referred to as wildfire-atmosphere interactions and is associated with unpredictable wildfire behaviour. Recent extreme wildfire events in Spain (2021) and Portugal (2017) that triggered pyro-convection spread significantly faster than predicted (Commissão Téchnica Independente, 2017; Castellnou et al., 2022), with some unexpectedly continuing to burn throughout the night despite worsening burning conditions. A well-documented and measured example is the first day of the Santa Coloma de Queralt (SCQ) fire in Catalonia~~on the 24th of July~~ , Spain, on July 24, 2021 (CFRS, 2022; Castellnou et al., 2022). The fire spread up to 4 times faster than predicted and unexpectedly continued burning into the night, maintaining a convective plume until midnight. The inability to extinguish these wildfires, combined with their unpredictability, results in dangerous situations for firefighters. Hence, in this study, we aim to enhance our understanding of ~~wildfire-atmosphere interactions through~~ the impact of pyro-convection ~~,~~ on the surrounding atmosphere using the SCQ fire as a case study, as it is a rare instance of an extreme wildfire event that has both well-documented fire behaviour and measured pyro-convection (Werth et al., 2016; Moisseeva and Stull, 2021).

Current operational fire behaviour models exclude the impact of pyro-convection (Kochanski et al., 2013) due to the poorly understood underlying physical connections to fire behaviour, despite the recognition of its importance since the 1950s (Byram, 1954; Davis, 1959). Based on a review of observational literature on convective wildfires, Potter (2012a, b) proposes that the upward mass flux due to pyro-convection increases the upwind surface inflow. It would explain the faster-than-predicted fire spread since operational models do not account for the increased upwind inflow due to pyro-convection. This agrees with recent in-plume ~~sounding~~ radiosonde measurements of pyro-convection, suggesting a significant correlation (R^2 = 0.9) between the pyro-convective strength and the mismatch between predicted and observed fire spread (Castellnou et al., 2022). The challenge with observations is their limited spatial and temporal extent, which inhibits simultaneously measuring ~~all wildfire-atmosphere interactions during~~ the full atmospheric modification driven by pyro-convection.

Turbulence-resolving Large-Eddy Simulation (LES) tools overcome this limitation by simulating pyro-convection in both space and time. Realistic LES studies of past wildfire events show that wildfires can modify the surrounding wind patterns (e.g. Peace et al., 2015, 2016; Filippi et al., 2018; Couto et al., 2024a; Roberts et al., 2024). The exact impact on the wind patterns varies between cases due to the varying ~~environmental~~ background conditions. This aligns with idealised LES studies, which show that ~~the~~ interactions between wildfires and the local airflow depend on ~~environmental~~ factors such as ~~the~~ fuel type (Coen et al., 2013) and ambient atmospheric stability (Sun et al., 2009). Despite the variability, the LES studies (Coen et al., 2013; Peace et al., 2016; Filippi et al., 2018) agree with the theory proposed by Potter (2012b) that wildfires can accelerate the ~~upwind inflow(Coen et al., 2013; Peace et al., 2016; Filippi et al., 2018)~~rear inflow, defined as the entrainment of air into the plume from behind the flaming zone.

In addition to the accelerated ~~upwind~~ rear inflow, the simulations by Coen et al. (2013) and Peace et al. (2016) show that wildfires can also modify the downwind airflow~~, creating~~. This creates frontal inflow, ~~a feature of~~ where air is entrained into the fire from ahead of the flaming zone. The creation of frontal inflow by pyro-convection is regularly used operationally to set backing fires ~~. This~~ and matches with Doppler measurements of convective wildfire plumes, which reveal significant frontal inflow into the fire ~~(Banta et al., 1992; Roberts et al., 2024)~~(Banta et al., 1992; Lareau and Clements, 2017; Roberts et al., 2024) . The measurements by Banta et al. (1992) suggest that the frontal inflow is part of a downwind wildfire-induced circulation consisting of the convection inside the plume, downwind downdrafts and the frontal inflow. The fire-induced circulation during convective wildfires could explain the continued nighttime burning, as observed during the SCQ fire. At night, downdrafts transport relatively warm and dry air to the surface, which would counteract the nighttime cooling and moistening of the atmosphere, thereby potentially mitigating the worsening burning conditions at night. Unfortunately, neither Coen et al. (2013) nor Peace et al. (2016) investigated the ability of fires to modify downwind burning conditions at night. Their simulations do not continue into the night, nor do they analyse the vertical airflow and subsequent impact on the thermodynamic structure of the atmospheric boundary layer during the downwind reversal of the surface winds.

Another remaining challenge with realistic LES studies of past wildfire events is their ~~validation~~evaluation. The dangerous conditions during convective wildfires limit the number of measurements (Sun et al., 2006). Consequently, realistic LES are mainly ~~validated~~ evaluated using observed fire perimeters~~and/or~~ , ambient weather observations, or a combination of both (e.g. Kochanski et al., 2013; Peace et al., 2015, 2016; Filippi et al., 2018; Campos et al., 2023). However, ~~a~~ the correctly simulated ambient weather or fire perimeter does not necessarily ensure an accurate simulation of pyro-convection. A recent study by Roberts et al. (2024) demonstrated that even with a prescribed fire perimeter (e.g. Couto et al., 2024b), the simulated pyro-convection and subsequent impact on the surrounding wind patterns did not match Doppler measurements of the kinematic plume structure. Hence, explicitly ~~validating~~ evaluating simulated pyro-convection is critical~~to advancing our understanding of wildfire-atmosphere interactions~~.

In this study, we developed an observation-driven LES of the SCQ fire using an in-plume sounding ~~measurements~~ provided by the Catalan Fire and Rescue Service (Castellnou et al., 2022). These measurements enabled us to ~~validate~~ evaluate the simulated pyro-convection by comparing the simulated and observed thermodynamic structure inside the fire-induced plume, which contrasts with Roberts et al. (2024), who focused on ~~validating~~ evaluating the kinematic plume structure. To our knowledge, soundings have not been previously used ~~for the validation of LES of~~ to evaluate simulated pyro-convection ~~, despite being increasingly used~~ in LES, despite their increasing use in operations to aid decision-making (Castellnou Ribau et al., 2025). Therefore, the first objective of this study is to demonstrate the ability of LES to reproduce in-plume ~~sounding observations~~ soundings of thermodynamic plume ~~structure~~ structures during extreme wildfire events. ~~Using the validated~~

Using the evaluated simulation, we pursue a twofold objective: (1) to study the impact of pyro-convection on the surrounding wind patterns proposed by Potter (2012b) and found by previous LES studies (Coen et al., 2013; Peace et al., 2016; Filippi et al., 2018); and (2) to analyse the impact of the ~~fire-driven~~ fire-modified wind patterns on the burning conditions by modifying the thermodynamic structure of the atmospheric boundary layer. To achieve these objectives, we ~~utilised MicroHH~~ used MicroHH (Van Heerwaarden et al., 2017) to simulate the SCQ fire, as it is a proven turbulence-resolving LES tool for simulating convective and pollution plumes (van Heerwaarden et al., 2014; Ražnjević et al., 2022), which enables a three-dimensional analysis of ~~wildfire-atmosphere interactions~~ the pyro-convection at the moment of the in-plume measurements. Furthermore, MicroHH allows for a landscape-scale domain (order of 10 km) while supporting a high resolution (order of 10 m). Hence, with MicroHH, we can simulate the large-scale ambient turbulent structures that define the atmospheric boundary layer while simultaneously resolving the small-scale turbulent structures inside the pyro-convective plume of the SCQ fire.

2 Methods

2.1 Santa Coloma de Queralt fire

The SCQ fire started on ~~the 24th of July~~ July 24, 2021 at 14 UTC (LT - 2) in Catalonia, Spain, with the ignition point located at 41.52329° N, 1.369071° E. It spread eastward under a predominantly westerly wind and directly developed a convective plume (Fig. 1a). Occasional overshooting created short-lived pyrocumulus clouds ~~, called overshooting pyrocumulus (oPyroCu),~~ between 17 and 19 UTC~~. The Catalan Fire and Rescue Service reports the arrival of the sea breeze at 17 UTC, explaining the formation of the oPyroCu(CFRS, 2022)~~, termed overshooting pyrocumulus (oPyroCu) by Castellnou et al. (2022). After 19 UTC, no further pyrocloud formation was observed ~~, which coincides with the stabilisation of the atmosphere during the day-to-night transition. It is expected that the stabilisation of the atmosphere limited the vertical extent of the plume, inhibiting the plume from reaching the lifting condensation level.Nevertheless~~(CFRS, 2022). The change from moist convection (i.e. pyrocloud formation) to dry convection (i.e. no pyrocloud formation) coincided with the arrival of the sea breeze at 19 UTC and sunset (19:41 UTC). The sea breeze caused the advection of moisture combined with backing of the wind from 300 to 240–270° (Fig. 1d). The moisture advected by the sea breeze, combined with the cooling around sunset, caused an increase in relative humidity (Fig. 1c). Nevertheless, observations indicate that the moistening did not result in renewed pyrocloud formation (Fig. 1a). Simultaneously, ~~the SCQ fire maintained a dry convective plume until midnight (22 UTC),~~ despite the cooling and moistening of the atmosphere around sunset (~~19:41 UTC;~~ Fig. 1c), the SCQ fire maintained a dry convective plume until midnight (22 UTC).

At 19:51 UTC, a ~~sounding as~~ radiosonde was released at the right flank of the fire (yellow star; ~~(~~Fig. 1a) into the convective plume of the SCQ fire that measured vertical profiles of temperature, ~~relative humidity~~specific humidity, wind speed and rising speed. ~~The measured profiles begin~~ A description of the equipment and measurement techniques is provided by Castellnou et al. (2022) . The radiosonde drifted predominantly eastward during its ascent (grey and red circles; Fig. 1a), with measurements starting at 80 m above ground level (~~e.g.~~ Fig. 1b). In ambient conditions, the maximum rising speed of a ~~sounding~~ radiosonde is ±2 m s^{-1}~~, which means that the sounding~~ . Rising speeds above 2 m s^{-1} indicate a vertical acceleration of the radiosonde by the convective motions of the wildfire plume (Castellnou et al., 2022). Hence, from the rising speed during the ascent of the radiosonde (Fig. 1b), we conclude that the radiosonde measured inside the convective ~~part of the plume between 0.2 and 1.4 km altitude (Fig. 1b). Besides measuring the plume during its ascent, a partial vertical~~ plume of the SCQ fire between 0.3 and

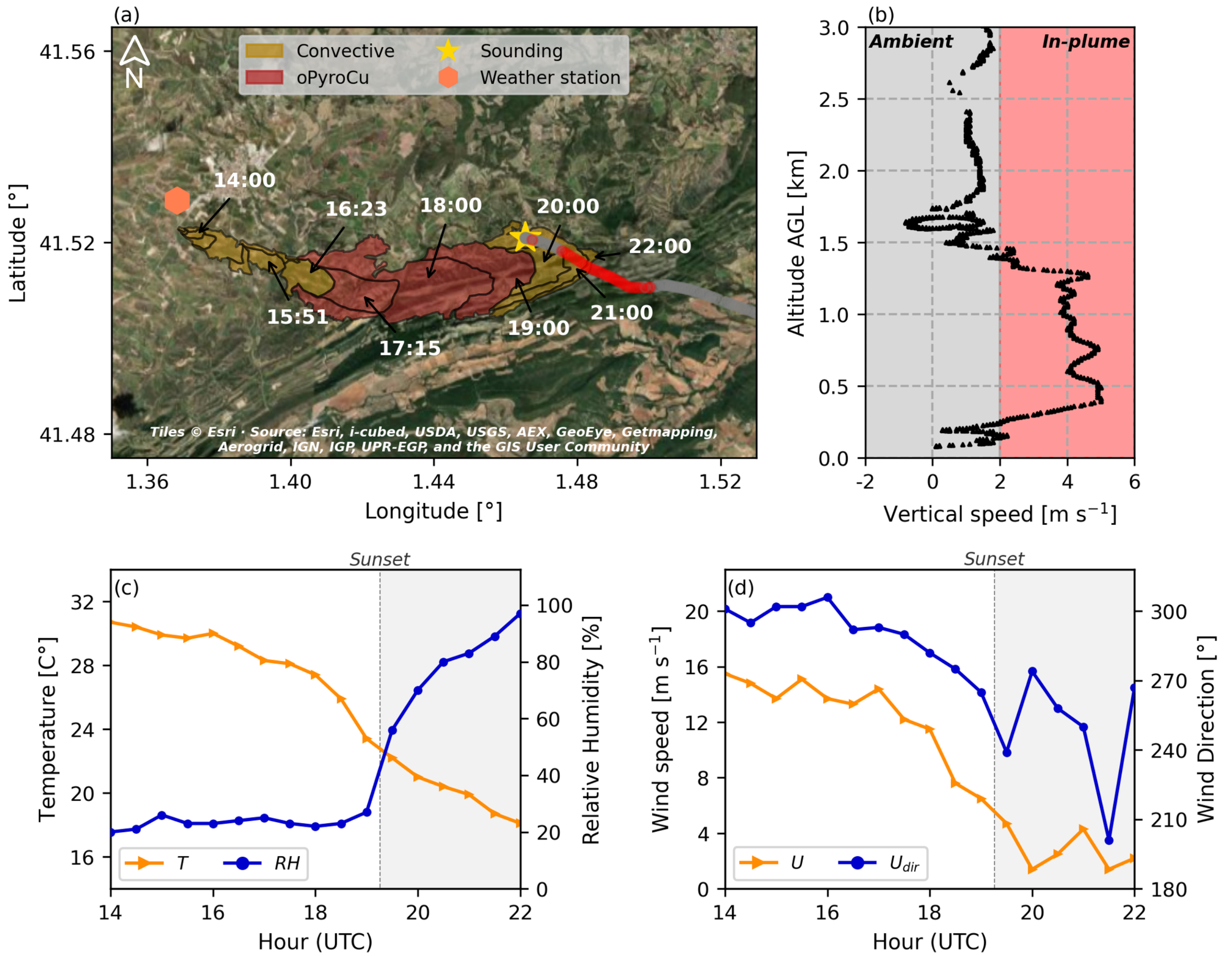

Figure 1. **(a)** The fire spread during the first day of the SCQ fire in UTC (LT - 2), including the locations of the sounding (star) and the synoptic weather station (hexagon). Additionally, the grey and red circles show the horizontal displacement of the radiosonde during its ascent. The red circles highlight the part of the ascent with rising speeds above 2 m s^{-1}, which indicates that at these locations the radiosonde was measuring within the convective core of the plume, since in ambient conditions, the maximum rising speed of a radiosonde is 2 m s^{-1} (Castellnou et al., 2022). **(b)** The rising speed of the ~~sounding that is used to determine~~ radiosonde during its ascent versus the altitude above ground level (AGL), with the grey and red shade indicating whether ~~a sounding is in~~ the radiosonde was out- or ~~outside~~ inside the convective plume based on ~~a~~ the 2 m s^{-1} threshold~~(red dotted line)~~. **(c)** The ~~diurnal~~ evolution of the temperature (T) and relative humidity (RH) during the SCQ fire measured by the synoptic weather station. **(d)** The same as **(c)** but for the 10 m wind speed (U) and direction (U_{dir}). The sounding ~~measurements~~ and synoptic observations are part of a larger observational dataset described by Castellnou et al. (2022). The fire perimeter map is an updated version of the map provided by Castellnou et al. (2022), ~~including~~ incorporating recent insights into the fire spread behaviour of the SCQ fire.

1.5 km altitude above ground level (AGL). In addition to measurements within the convective plume, the radiosonde recorded a partial profile of the ~~environment was measured~~ ambient temperature and relative humidity during its descent~~around 20:30 UTC (not shown).~~ .

Consequently, we ~~can validate~~ will use the radiosonde measurements to evaluate both the simulated ~~convective plume and the environment with the sounding measurements .~~ pyro-convection and the ambient conditions in which the pyro-convection was simulated. For the evaluation, we will focus on comparing the observed and simulated temperature profiles. Furthermore, we will also compare the measured wind speed in the convective plume with the simulated wind speed. The measured wind speed during the descent of the radiosonde in the surroundings of the plume and the measured specific humidity are not used for the comparison. We consider the wind speed measurements during descent unreliable due to the high descent speed of the radiosonde ($8-9$ m s^{-1}). The specific humidity measurements, on the other hand, are reliable but redundant for evaluating our simulation, as both observations and the simulation indicate a dry convective plume (i.e., no pyro-clouds). Hence, the simulation was sufficiently dry.

2.2 Simulation setup

This study focuses on correctly simulating and exploring the impact of pyro-convection on the atmosphere. Hence, in our simulation setup, we prioritise atmospheric realism while significantly simplifying the simulated fire behaviour to isolate the impact of the fire on the atmosphere.

To analyse the impact of the SCQ fire on the atmosphere, we performed two four-hour simulations of ~~the 24th of July~~ July 24, 2021 (16–20 UTC) with MicroHH (Van Heerwaarden et al., 2017): one without a fire, *ref-run*, and one with a fire, *fire-run*.

Table 1. An overview of the main simulation parameters of MicroHH (Van Heerwaarden et al., 2017). The full simulation setup to reproduce this study is provided in the associated data repository (Roelofs et al., 2025).

Parameter	
Domain size	38 400 × 25 600 × 12 082 m
Horizontal resolution	25 m
Lowest vertical level	10 m
Vertical stretching levels	3 000 m, 12 082 m
Vertical stretching factor	1.002, 1.015
Initial and boundary conditions	ERA5 reanalysis (41.51775 °N, 1.494428 °E)
Simulation period	16:00–20:00 UTC, July 24, 2021
Advection scheme	2i5 (2nd-order with 5th-order interpolation)
Surface scheme	surface (Monin-Obukhov based surface model)
Roughness length momentum	0.075 m
Roughness length heat	0.003 m

The difference between the *ref-run* and the *fire-run* shows the impact of the SCQ fire. We use the last hour of the simulations (19–20 UTC) for the analysis as it matches the timing of the sounding measurement (19:51 UTC). The first two hours serve as spin-up time, after which the fire is initialised in the *fire-run*. This provides an additional hour of spin-up time (18–19 UTC) to allow the convective plume to develop, ensuring a convective plume between 19 and 20 UTC.

The generic setup of MicroHH for both runs is provided in Table 1 and the specific implementation of the fire and the meteorological boundary conditions is provided in Sects. 2.2.1 and 2.2.2, respectivelly.

2.2.1 Fire implementation

To implement a fire in MicroHH during the *fire-run*, we added a stationary moon-shaped area with a constant heat flux of 145 kW m^{-2} (Fig. 2) between 18 to 20 UTC on top of the ambient surface fluxes from ERA5 (see Sect. 2.2.2). To prevent numerical errors, we applied Gaussian smoothing (σ = 25 m) to smooth the transition from the ambient surface fluxes ($\sim$ 1–10^2 W m^{-2}) to the fire fluxes ($\sim$ 10^5 W m^{-2}). The stationarity is justified by the significantly smaller rate of spread of the fire compared to the wind speed, which makes the movement of the fire negligible from an atmospheric perspective, the main focus of our study. The significant advantage of stationarity is that it enables temporal averaging of the plume to detect consistent patterns in the impact of the SCQ fire on the atmosphere. Additionally, stationarity eliminates the need for fuel and topographic maps. Hence, the surface of the simulated domain is flat and homogeneous. Although the local topography is simplified to a flat plain, the average elevation is accounted for through the ERA5 pressure field (see Sect. 2.2.2).

The moon-shaped area is based on observations by the Catalan Fire Service, including the fire perimeters shown in Fig. 1a, which indicate a fire 1100 m wide and 350 m deep, with a 150 m deep flaming zone at the head of the fire (arrows 1,2 and 3 in Fig. 2). To implement it, we define the shape based on two quadratic equations, Eqs. (1) and (2), which represent the east and west borders of the flaming zone, respectively:

$$x_{east}(y) = x_0 + L_{east}\left[1 - \left(\frac{(y - y_c)}{\frac{W}{2}}\right)^2\right] \quad (1)$$

$$x_{west}(y) = x_0 + L_{west}\left[1 - \left(\frac{(y - y_c)}{\frac{W}{2}}\right)^2\right] \quad (2)$$

with x_0 representing the distance of the fire to the west border of the domain (2000 m), y_c representing the centre of the fire on the y-axis (12812.5 m) and W the width of the fire (arrow 1 in Fig. 2; 1100 m). Lastly, L represents the distance between x_0 and the peak of the parabole at y_c, so for the west border (L_{west}) of the flaming zone (Eq. 2) it represents arrow 2 in Fig. 2 (350 m), while for the east border (L_{east}) it represents arrows 2 + 3 (500 m).

The flaming zone is defined as the area between Eqs. 1 and 2 where $x_{west} \leq x \leq x_{east}$. At the flanks of the fire where $y - y_c = \pm\frac{w}{2}$, the dimensional ratio $\left(\frac{(y-y_c)}{\frac{W}{2}}\right)^2$ = 1. Hence, $x_{west} = x_{east}$ at the flanks, therefore resulting in the end of the flaming zone. When moving from the flanks to the centre of the fire ($y = y_c$), the dimensional ratio goes to 0, resulting in the maximum difference between Eqs. 1 and 2, which equals $L_{east} - L_{west} = 150$ m, the maximum flaming zone depth (arrow 3 in Fig. 2).

Furthermore, the constant heat flux means that we do not explicitly simulate the combustion. Instead, we derived the fire line intensity (FLI in kW m^{-1}) based on Byram's definition of the fire line intensity (Byram, 1959):

$$FLI = 0.5H\,[w\,(1.0308 - 0.048FFMC)]\,ROS \tag{3}$$

where ROS represents the observed rate of spread m s^{-1} determined from the observed fire perimeter (Fig. 1a) using the methodology described by Duane et al. (2024), H the heat content of the fuel in J kg^{-1} and w the amount of available fuel in kg m^{-2}. For H, we used an effective heat content of 14,700 kJ kg^{-1}, which is within the average reported H for experiments (Finney et al., 2021). Furthermore, we added two correction factors. Firstly, following Rio et al. (2010), we applied a correction factor of 0.5 based on the assumption that 50% of the radiative heat is lost to the surrounding atmosphere, meaning that only 50% of the FLI contributes to the buoyant plume formation. Secondly, similarly to Lareau and Clements (2016), we correct the available fuel based on the fine fuel moisture content, $FFMC$ (Nelson, 2000), albeit with a different approach. The $FFMC$ correction factor in Eq. (3), $1.0308 - 0.048FFMC$, is designed under the assumption that all fuel is available for burning at a relative humidity of 3%, and that the amount of available fuel decreases linearly with increasing relative humidity until the extinction relative humidity of 21% is reached.

For the Santa Coloma de Queralt fire (between 19 and 20 UTC), the ROS is determined at 1 m s^{-1}, and w was approximated at 3.3 kg m^{-2} based on the dominant fuel type, the pinus halepensis. Furthermore, we estimated the $FFMC$ to be between 0 and 6% based on the weather station data (Fig. 1). Using Eq. (3), this results in an FLI ranging from 18*10^3 to 25*10^3 kW m^{-1}. To convert the FLI into a surface flux, we divided the FLI by the flaming zone depth (150 m, arrow 3 in Fig. 2), which resulted in a fire heat flux ranging between 120 and 170 kW m^{-2}. Within this range, we selected the mean heat flux of 145 kW m^{-2} for the fire in our simulation.

Lastly, we do not simulate the chemical composition of the fire-induced plume. Instead, we use an inert tracer to represent the plume shape. Consequently, we do not simulate the interaction of the smoke plume with radiation, so shadowing effects are not included. The lack of shadowing effects is expected to have a negligible impact on the outcomes of this study as we focus on the period between 19 - 20 UTC, which is around sunset (19:41 UTC). At sunset, the incoming radiation makes a minimal contribution to the energy balance, rendering the shadowing effect negligible.

2.2.2 Meteorological boundary conditions

To create as realistic meteorological conditions as possible in MicroHH, we ~~use~~ used the ERA5 reanalysis data (Hersbach et al., 2020) as boundary conditions. ERA5 is considered one of the best currently available reanalysis datasets for studying convective environments (Taszarek et al., 2021). Additionally, the high vertical resolution (28 layers within the lower 2 km of the atmosphere) of ERA5 at ~~an hourly interval means that it~~ hourly intervals captures the pre-fire atmospheric boundary layer,

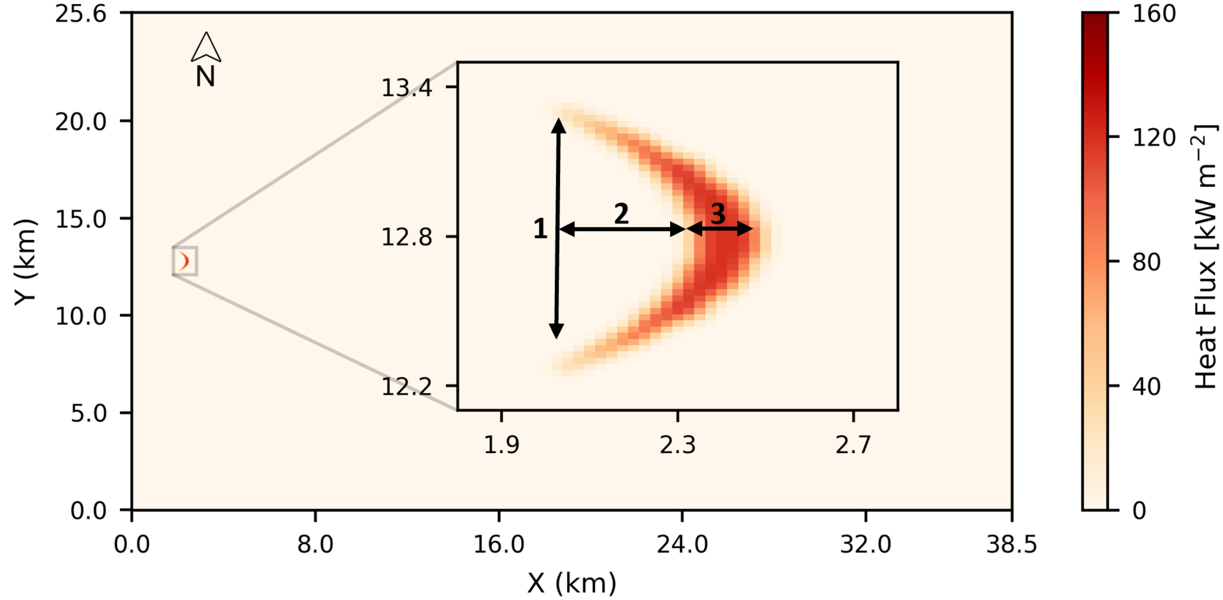

Figure 2. The boundary conditions for MicroHH of θ_v **(a)**surface heat flux in the simulation, q **(b)**including Gaussian smoothing (σ = 25 m), U **(c)** and U_{dir} **(d)** obtained from with a zoom-in on the ERA5 reanalysis dataset (Hersbach et al., 2020) at 16moon-shaped implementation of the fire. The arrows indicate the dimensions of the implemented wildfire, 18 which are 1100 m (1), 350 m (2), and 20 UTC150 m (3).

which is the layer where the pyro-convection occurs. The We retrieved the ERA5 data is retrieved at boundary conditions at a single point, the centre of the SCQ fire (latitude: 41.51775°, longitude: 1.494428°), since MicroHH uses periodic boundaries.

Figure 3 shows the ERA5 boundary conditions of the virtual potential temperature (θ_v), specific humidity (q), wind speed (U) and wind direction (U_{dir}) at 16, 18 and 20 UTC. The q and U_{dir} show moistening of the CBL combined with backing winds, indicating a sea breeze in ERA5 after 16 UTC (Fig. 3b,d). Besides moistening, the sea breeze also causes cooling of the boundary layer, which combined with the shift from a positive to a negative surface heat flux between 19 and 20 UTC explains the transformation of the convective boundary layer at 16 UTC (blue line; Fig. 3a) into a neutral boundary layer (0 < z < 0.5 km) capped by a residual layer (0.5 < z < 2 km) between 19 and 20 UTC (purple dotted line; Fig. 3a), the period of interest for this case study of the SCQ fire. The reduction in turbulence is also visible in the vertical profile of U, which shows the development of a low-level jet at 20 UTC (purple dotted line; Fig. 3c).

The arrival of the sea breeze in ERA5 (after 16 UTCaligns with the observations of the Catalan fire and rescue service described above.However, the) occurs three hours earlier than the observations (see Sect. 2.1). Furthermore, the sea breeze in ERA5 is accompanied by significant backing of the wind in ERA5 is stronger than the observations by the local fire service, which indicate that even after the sea breeze arrived, the fire continued to advance eastward under the influence of westerly winds . We expect that the difference with the observations originates from the (±90°), resulting in southerly winds (Fig. 3d), while the observations indicate only slight backing of the wind by 30 km resolution of to 60° (Fig. 1d), which kept the winds

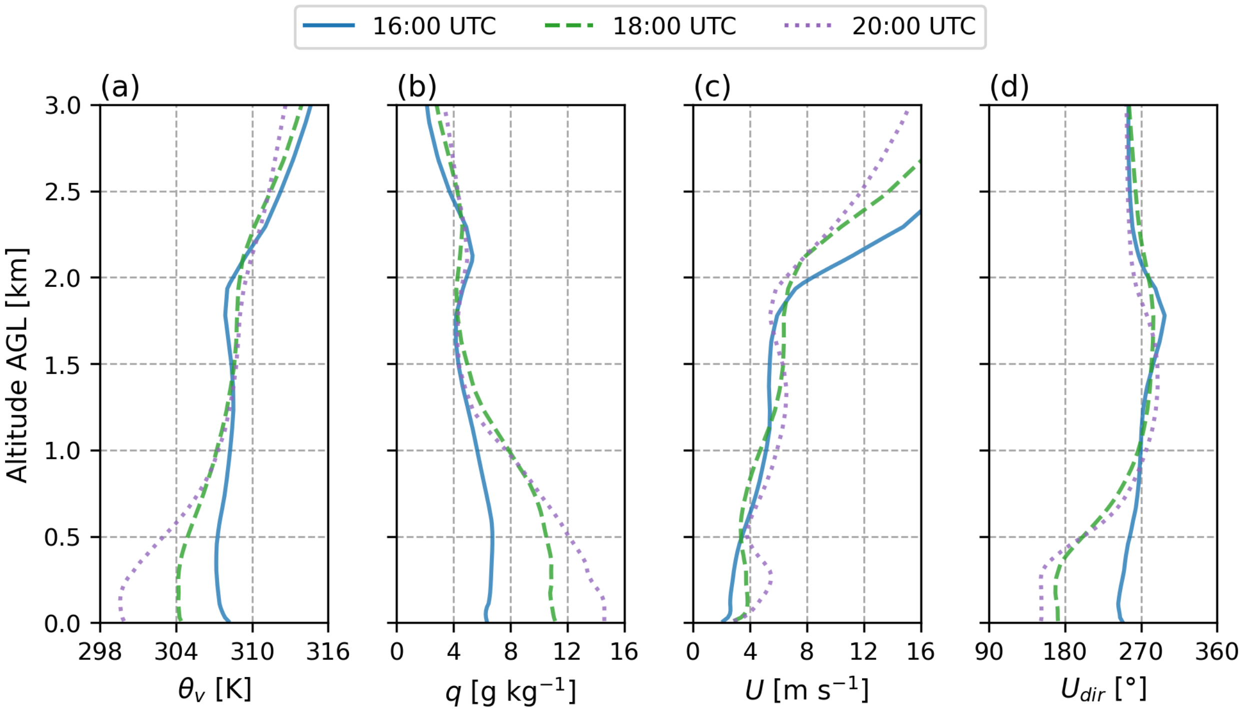

Figure 3. The boundary conditions for MicroHH of θ_v **(a)**, q **(b)**, U **(c)** and U_{dir} **(d)** obtained from the ERA5 reanalysis dataset (Hersbach et al., 2020) using the (LS)^{2}D python package (van Stratum et al., 2023) at 16, 18 and 20 UTC.

predominantly westerly. Previous validation studies of ERA5 ~~, which~~ in complex terrain show that a horizontal resolution of 31 km is often insufficient to resolve small-scale orographic features, leading to significant discrepancies in local winds (Gualtieri, 2021; Zuo et al., 2025). For the SCQ fire, this suggests that the ERA5 grid is too coarse to resolve the ~~small-scale variations in wind direction due to the complex local topography. This is a common challenge with reanalysis products such as~~ coastal mountain range in Catalonia, which acted as a barrier to the sea breeze, delaying its arrival until 19 UTC (CFRS, 2022) . Despite the temporal and directional mismatch between the sea breeze in ERA5 ~~, but~~ and the observations, it does not ~~affect the simulated fire behaviour, as we assume~~ significantly affect the objectives of our study, since we simulate a stationary fire~~(detailed below). This~~ , meaning the location of the fire inside our simulation is decoupled from the ambient wind direction. This decoupling allows us to focus on understanding the impact of pyro-convection on the atmosphere rather than accurately replicating the observed fire ~~behaviour~~spread under imperfect boundary conditions.

~~MicroHH uses~~ The periodic boundary conditions ~~, meaning~~ of MicroHH require the simulated domain ~~should~~ to be large enough to prevent unwanted recirculation of the wildfire-induced plume. Since the observations indicate a predominantly eastward development of the plume, we elongated the domain eastward. This resulted in a domain of 38.4 km × 25.64 km × 12 km (x × y × z; Fig. 2) with an equidistant horizontal resolution of 25m and a stretched vertical resolution starting at 10 m near the surface . Preliminary analysis showed that this domain size prevents unwanted recirculation of heat and moisture (see).

To implement a fire within MicroHH, a surface area with increased sensible and latent heat flux is added. To represent the SCQ fire, we implemented a moon-shaped surface area measuring 1100m in width and 150 m in depth combined with a 145 kW m^{-2} sensible heat flux (Fig. 2). The simulated fire also emits an inert tracer to visualise the simulated pyro-convection. To prevent numerical errors, we applied Gaussian smoothing (σ = 25 m) to smooth the transition from the environmental fluxes ($\sim$ 1–10^2 W m^{-2}) to the wildfire fluxes ($\sim$ 10^5 W m^{-2}).

With this approach of implementing the SCQ fire into MicroHH, we made two significant simplifications: (1) we presume the fire to be stationary; (2) we use prescribed surface fluxes from the ERA5 reanalysis data surrounding the fire to negate the need for a radiation scheme. The stationarity is justified by the significantly smaller rate of spread of the fire compared to the wind speed, which makes the movement of the fire negligible from an atmospheric perspective. Furthermore, by using prescribed surface fluxes, we inherently neglect the plume shadowing effects in our simulations, which consequently removes the need to simulate the aerosol composition of the plume. The lack of shadowing effects is expected to have a negligible impact on the outcomes of this study as we focus on the period above the surface (Table 1). Figure 4 shows that there is no significant difference in θ_v at the borders of the domain between 19 – and 20 UTC, which is around sunset (19:41 UTC). At sunset, the incoming radiation makes a minimal contribution to the energy balance, rendering the shadowing effect negligible. While these simplifications reduce the realism of certain aspects of the simulations (i.e. fire behaviour and radiation), they also reduce the complexity and uncertainty of the simulations, thereby facilitating the main objective of this study: assessing the impact of pyro-convection on the surrounding atmosphere. In agreement with θ_v, the vertical profiles of q show no significant differences either (Fig. A1). Hence, the elongated domain is sufficiently large to prevent recirculation of the wildfire-induced plume.

3 Results

The outcomes of this study are presented per objective. First, we compare the simulation with the visual observations and in-plume sounding measurements of the SCQ fire. Second, we analyse the impact of pyro-convection on the wind patterns and, subsequently, the thermodynamic structure of the atmospheric boundary layer surrounding the SCQ fire.

3.1 ValidationComparison with observations

To validate evaluate the simulated pyro-convection between 19 and 20 UTC, we compared compare the simulated plume shape and vertical profile of the virtual potential temperature (θ_v) with the observations in and wind speed (U) with visual observations (Fig. 5and) and the in-plume radiosonde measurements (Fig. 6, respectively). The observed plume of the SCQ fire between 19 and 20 UTC is presented in Fig. 5a-c for 19:13, 19:34 and 19:59 UTC. Throughout the hour, a well-developed convection column was present observed (1) with occasional overshooting (2) and a horizontally dispersed smoke layer, also called the dispersion layer (3). Here, the distinction between the convection column and the dispersion layer is made visually

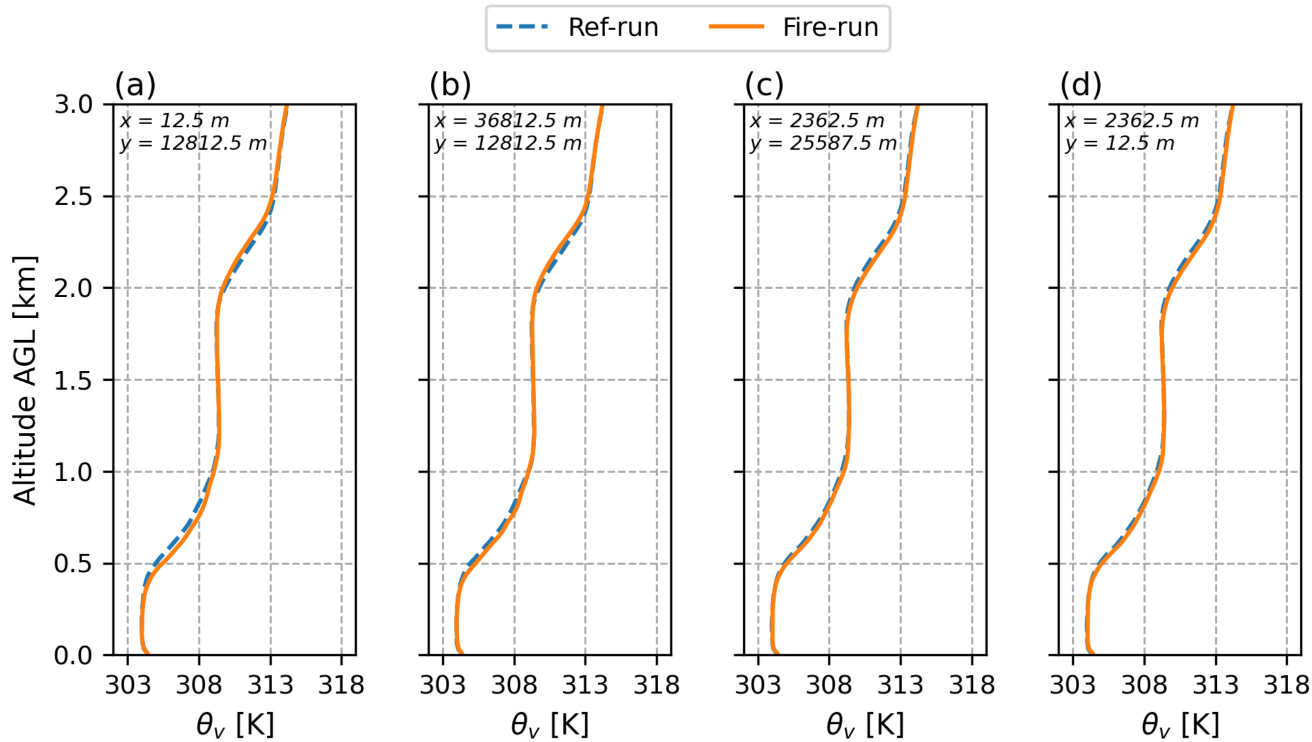

Figure 4. The normalised surface heat flux in averaged vertical profiles of θ_v between 19 and 20 UTC for the simulation using the maximum fire intensity without (145 kW m^{-2} *ref-run*; blue dashed line) and with a zoom-in on fire (*fire-run*; orange line) at the moon-shaped implementation four borders of the firedomain: west **(a)**, east **(b)**, north **(c)**, and south **(d)**. The arrows numbered one to three x and y values on top of each column indicate the dimensions exact location of the implemented wildfire, which are 1100 m, 350 m, and 150 m, respectivelyvertical profiles following the coordinate system shown in Fig. 2.

based on the dominant axis of development: vertical (i.e., convection column) or horizontal (i.e. dispersion layer). The average simulated plume shape between 19 and 20 UTC based on the inert tracer is shown in Fig. 5d (grey outline). Similar to the observed plume, the average simulated plume also shows a convection column and a dispersion layer. Occasional overshooting also occurs in the simulation (not shown), but not consistently enough to affect the average plume shape. Additionally, the simulation shows, on average, downward transport of smoke below the dispersion layer, which suggests subsiding motions ahead of the fire front. Although the downward transport of smoke does not become apparent in Fig. 5a-c, it does match descriptions of the plume behaviour provided by local fire fighters.

To quantify the observed plume shape, we combined the measured rising speed and displacement of the in-plume sounding (black triangles; For the remainder of this comparison, we will compare the radiosonde measurements to the simulation, which has two challenges. Firstly, the location of the radiosonde relative to the plume during the measurements is unknown, as we do not have observations on the exact location of the plume during the sounding. Secondly, we cannot replicate the exact shape

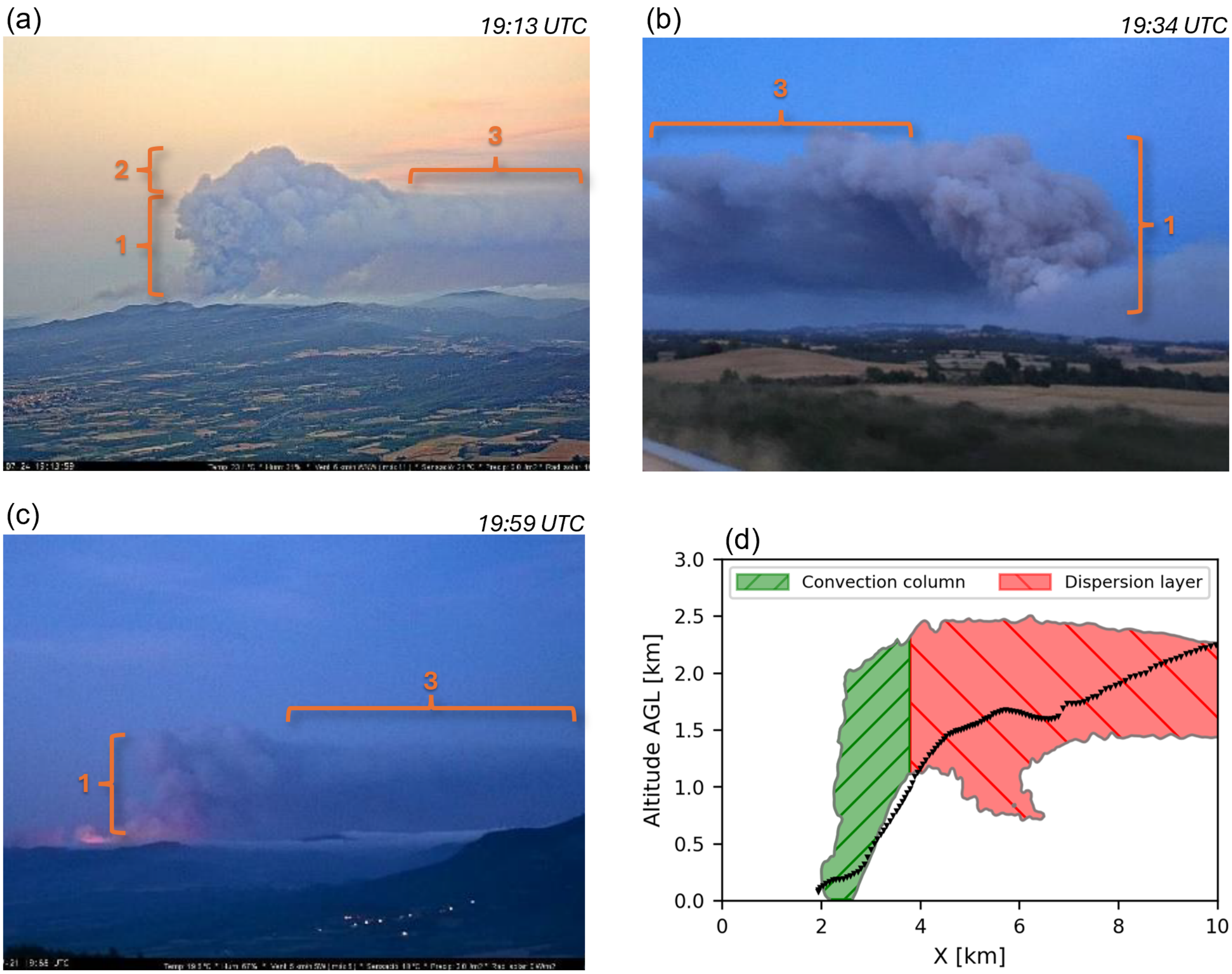

Figure 5. A qualitative comparison between the observed and simulated plume shape between 19 and 20 UTC. The observed plume is presented before sunset (19:41 UTC) at 19:13 **(a)** and 19:34 **(b)** and after sunset at 19:59 **(c)** UTC (LT - 2) with the convection column, occasional overshooting and dispersion layer indicated by the numbers 1 to 3, respectively (Pictures taken from Ribau et al. (2022)). The average simulated plume shape between 19 and 20 UTC **(d)** is visualised using the inert tracer (> 0.0025) with ~~the~~ green and red shading indicating the convection column and dispersion layer, respectivelly. Additionally, the displacement of the ~~sounding~~ radiosonde in the east-west direction is shown (black triangles).

of the turbulent plume at the time of the sounding, since turbulence is a chaotic process. Instead, we can replicate the average shape of the plume between 19 and 20 UTC, the period in which the sounding was released. Despite these challenges, we know that the radiosonde moved predominantly eastward (Fig. ~~5d) . The rising speed indicated that the sounding was inside the convection column~~ 1a) and that it measured inside the convective core of the plume between 0.3 and 1.5 km ~~, as its rising speed exceeded 2 m s^{-1}~~ altitude (Fig. 1b). ~~The~~ To capture the convective core of the plume in the simulation, we extract a xz cross-section at y = 12.8125 km. This xz cross-section represents an east-west plane through the centre of the fire, matching the predominant eastward movement of the radiosonde. Hence, we will compare the radiosonde measurements with the averaged xz cross-section of the plume between 19 and 20 UTC through the centre of the fire.

The measured rising speed and horizontal displacement of the ~~sounding~~ in-plume radiosonde (black triangles; Fig. 5d) ~~between these altitudes~~ provide a quantification of the observed plume shape. The horizontal displacement of the radiosonde within the convective core of the plume (0.3 - 1.5 km altitude) shows that the ~~simulated convection column up to 1.5 km~~ averaged simulated plume shape is less tilted than ~~observed~~the observed one. Above 1.5 km, the rising of the ~~sounding~~ radiosonde effectively halts, resulting in approximately 3 km of primarily horizontal displacement between 1.5 and 1.7 km altitude before continuing its ascent (Fig. 5d). This suggests that the ~~sounding~~ radiosonde exited the convection column between 1.5 and 1.7 km, but whether this was at the top of the plume cannot be derived from the rising speed and displacement of the ~~sounding~~radiosonde.

To further ~~validate the simulated SCQ fire, we compared the simulated~~ evaluate the simulated pyro-convection, we compare the simulated in-plume θ_v ~~inside the plume and the environment with the measured θ_v during the ascent and descent of the sounding, respectively~~ and U, with the radiosonde measurements during its ascent (black triangles; Fig. 6). Additionally, we evaluate the simulated ambient conditions by comparing the observed θ_v during the descent of the radiosonde. The measurements near the surface (< 0.3 km) during the ascent show an increase in θ_v (Fig. 6b). This increase coincides with the near-surface acceleration of the rising speed (Fig. 1b), which indicates that ~~it~~ the increase in θ_v reflects the transition from the ~~environment into the~~ ambient atmosphere into the convective plume. Between 0.4 and 1.4 km, a relatively constant θ_v of 308 K is observed, which coincides with the observed convection column (i.e. where rising speed > 2 m s^{-1}). Above the well-mixed layer, an inversion is found (1.7 ~~–~~ – 1.9 km) with a stable layer on top (> 1.9 km), which explains the predominantly horizontal displacement of the ~~sounding~~ radiosonde for 3 km between 1.5 and 1.7 km altitude (Fig. 5d). The ~~same inversion and the stable layer are also captured during the descent of the sounding~~ inversion is also visible in the measured U profile inside the plume (Fig. 6~~a). During the descent, the sounding measured the environmental conditions. Consequently, the measurements during the ascent above 1.5 -~~ c). The U is relatively constant (5 – 10 m s^{-1}) up to 1.7 km ~~represent the ambient conditions. Therefore, to validate the simulated plume, we compared the observed vertical profile of θ_v during the ascent between 0.4 and 1.5 km with the simulated θ_v inside the convection column.~~

~~A direct comparison of the simulation with the measured θ_v is impossible since the observed convection column was ± 30% more tilted than the simulated convection column~~ above which it increases, indicating the transition from the atmospheric boundary layer into the free troposphere. The same inversion and stable layer are captured in the surroundings of the plume during the descent of the radiosonde (Fig. ~~5d). Consequently, the measurement locations (black triangles) do not align with the average location of the simulated convection column (green shaded area). To circumvent this mismatch, we~~ 6a).

We compared the observations with the median θ_v and U profile (blue line) inside the average simulated convection column ~~. The median~~ (Fig. 6). The medians of θ_v ~~is~~ and U are determined per height inside the green-shaded area based on the averaged xz cross-section ~~of θ_v~~ at y = 12.8125 km. The spread in θ_v and U is indicated with the first and third quantiles (blue dotted lines). For consistency, the same approach is used to ~~validate the simulated environment~~compare the measured and simulated ambient conditions surrounding the fire-induced plume, except for using the *ref-run* instead of the *fire-run* and the median based on the entire xz cross-section instead of the green-shaded area.

Figure 6b shows the median profile of θ_v inside the average convection column up to 2.3 km, which is the average height of the convection column between 19 and 20 UTC (Fig. 5d). At the surface (z = 10 m), the median θ_v reaches 384 K (not shown), which quickly decreases due to mixing with the colder ambient air (304 K). This pattern is opposite to the sounding

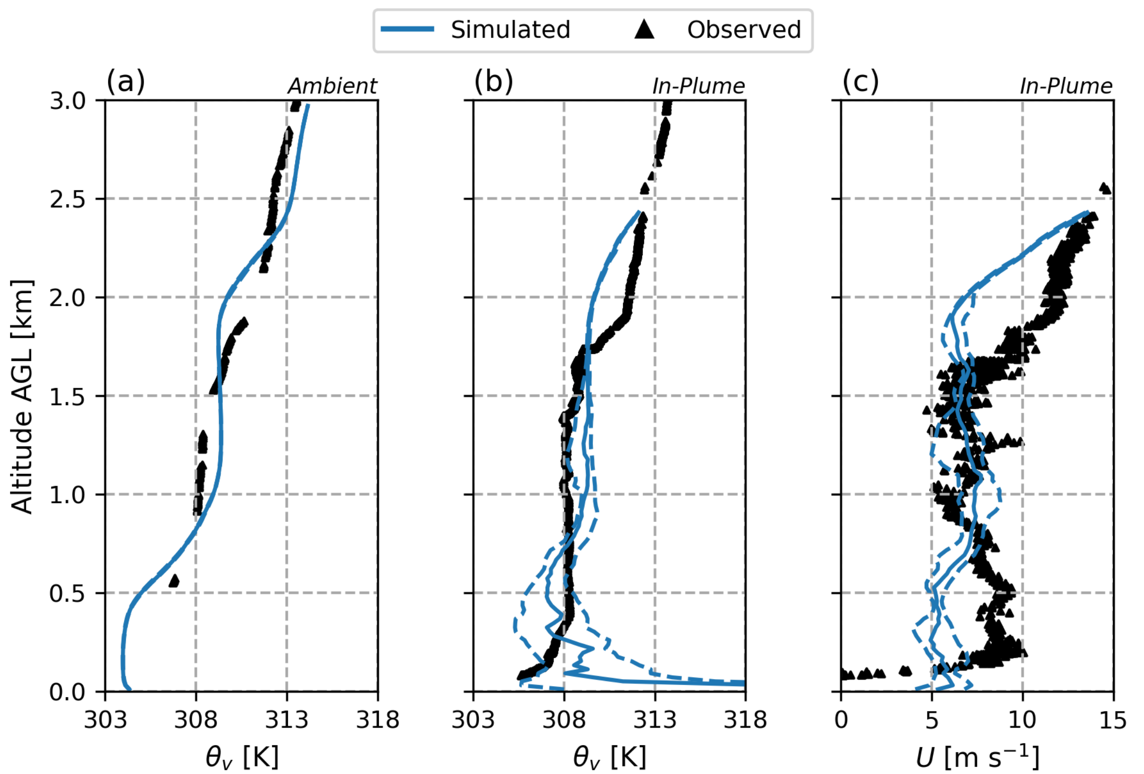

Figure 6. The vertical profiles θ_v measured during the descent (~~environment~~ambient conditions) and ascent (in-plume) of the ~~sounding~~ radiosonde compared to the median simulated θ_v in the ~~average environment~~ surrounding **(a)** and inside the average convection column **(b)** between 19 and 20 UTC. **(c)** The same as in **(b)** but for the measured and simulated wind speed, U. The first and third quantiles (blue dashed lines) indicate the simulated variability.

~~observations~~ (black triangles), which ~~show~~ shows a decrease in θ_v near the surface, because the simulated profile starts inside the flaming zone, whereas the ~~sounding~~ radiosonde was launched outside ~~at the flank of the~~ the flaming zone.

Above the rapid decrease in θ_v, we find a well-mixed layer with a θ_v varying between 307 and 310 K in the simulation, which matches the observed mixed layer θ_v of 308 K (black triangles). However, the inversion capping the well-mixed layer is simulated $\pm$ 0.3 km higher than observed (1.7 km). A similar overestimation is visible for the U profile. The simulated U is relatively constant up to 2 km altitude before increasing, indicating the presence of an inversion in the simulation at 2 km, while the observed U indicates an inversion at 1.7 km altitude.

The same difference in inversion height is present in the ~~environment~~ surroundings of the plume (Fig. 6a).

~~The environmental conditions of~~ The ambient conditions in the simulation are based on the ERA5 boundary conditions (Fig. 3), which also overestimate the inversion height by 0.3 to 0.4 km. Hence, the inversion height mismatch between the observations and the simulation (Fig. 6a) is created by ERA5 and does not reflect the performance of MicroHH. The overestimation by ERA5 is consistent with measurements in the same region and period of the SCQ fire presented by Mangan et al. (2023). They showed a consistent overestimation of the convective boundary layer by ERA5 due to ~~the inability of ERA5 to capture the~~ its inability to capture local surface heterogeneity. At night, this would result in an overestimation of the height of the residual layer, which we find in Fig. 6a.

Due to the overestimated inversion height, we conjecture that the simulation also overestimates the plume height. A higher plume could amplify the impacts of wildfire-induced pyro-convection on the surrounding kinematic and thermodynamic ~~environment~~structure of the atmosphere. Nonetheless, it is not expected to significantly alter the outcomes of this study, since we aim to explore the physical mechanisms behind the impacts of pyro-convection on the kinematic and thermodynamic structure of the atmosphere. In future studies, we will systematically quantify how, among others, the boundary layer structure alters the impact of pyro-convection on the atmosphere.

3.2 Fire-modified wind patterns

To investigate how the SCQ fire impacts its surrounding wind patterns, we compare the *fire-run* with the *ref-run*. The direct impact of any wildfire on the atmosphere is the creation of buoyancy by heating the air. For the SCQ fire, we find average vertical velocities up to 3 m s^{-1} at the surface (Fig. 7b), an order of magnitude larger than the ~~environmental~~ ambient vertical velocities (Fig. 7a). To sustain the increased vertical airflow above the flaming zone (black dotted line), additional inflow into the flaming zone is needed. Figure 7b suggests two mechanisms that could provide the additional inflow: (1) downdrafts at the southern and western borders of the flaming zone and (2) horizontal inflow from the western, eastern and northern borders (grey streamlines).

To quantify the change in airflow, we calculate the mass balance of the red box surrounding the flaming zone (Fig. 7) between 0 and 60 m altitude ~~, thereby focusing on the airflow changes in the~~ (Fig. 8). For the mass balance, we follow the mass conservation definition within MicroHH as defined in Eq. (2) in Van Heerwaarden et al. (2017), which uses a reference density that is a function of height only. The limited altitude (< 60 m) focuses the analyses on the near-surface layer below the plume neck~~(Fig. 8).~~ .

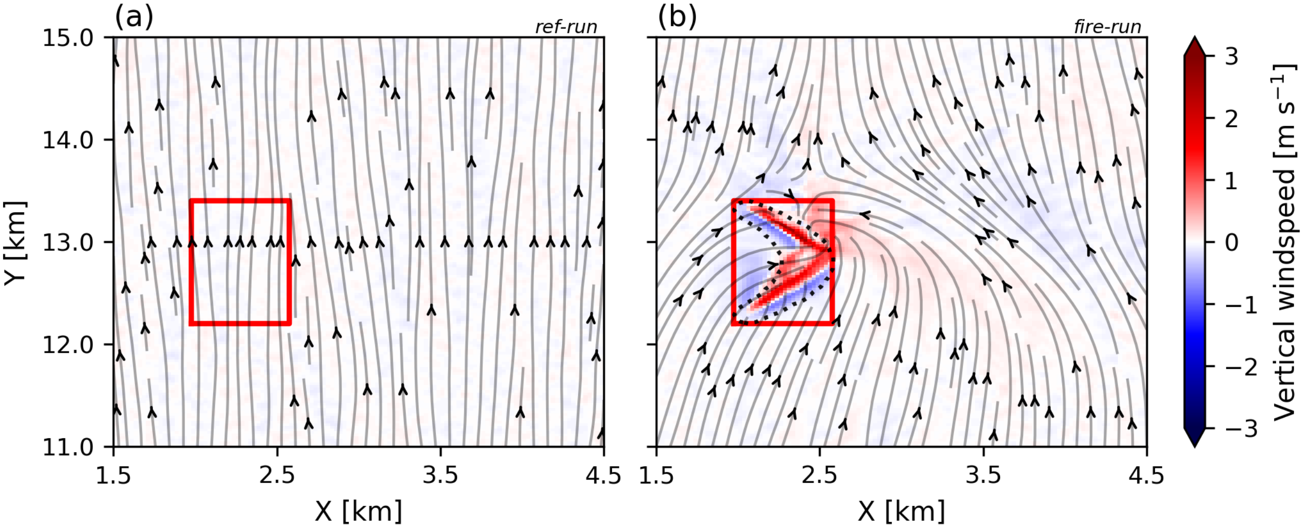

Figure 7. The average vertical wind speed in the *ref-run* **(a)** and *fire-run* **(b)** between 19 and 20 UTC at the lowest vertical level of the simulation (z = 10 m). The grey streamlines show the hourly-averaged horizontal airflow patterns, the magnitude of which is presented in Fig. 9a,c. Furthermore, the red rectangle is the area for which we calculated the mass balance to quantify the influence of the SCQ fire on the surface winds (Fig. 8), and the black dotted line **(b)** indicates the simulated flaming zone of the SCQ fire (Fig. 2).

Without the SCQ fire (*ref-run*), we find that the vertical in- and outflow are balanced (149×10^3 and -145×10^3 kg s^{-1}, respectively). Additionally, as expected, the horizontal part of the mass flux balance of the *ref-run* is dominated by the ~~mean wind pattern that is the effect of a~~ southerly sea breeze, with predominantly inflow from the south (131×10^3 kg s^{-1}) and a nearly equal outflow in the north (-132×10^3 kg s^{-1}).

Comparing the *ref-run* with the *fire-run* in Fig. 8, we find a 620×10^3 kg s^{-1} increase in vertical outflow, which is partially compensated by a 273×10^3 kg s^{-1} increase in vertical inflow. The gap between the changes in vertical in- and outflow (347×10^3 kg s^{-1}) is covered predominantly by changes in the airflow over the northern and western borders ($+129\times10^3$ and $+176\times10^3$ kg s^{-1}, respectively). At the northern border, the SCQ fire increases the inflow while decreasing the outflow, changing it from a net outflow border (-132×10^3 kg s^{-1}) to an almost net zero border. At the western border, the fire predominantly increases the inflow ($+145\times10^3$ kg s^{-1}). Consequently, the net vertical outflow induced by the SCQ fire (-343×10^3 kg s^{-1}) is mostly compensated by southern (172×10^3 kg s^{-1}) and western (168×10^3 kg s^{-1}) inflow.

The total mass flux balance for the *fire-run* does not indicate a significant contribution from the eastern border, the front of the SCQ fire, despite the streamlines suggesting significant changes in airflow at the eastern border due to the fire (Fig. 7). This contradiction arises because both the in- and outflow at the eastern border increase equally, effectively cancelling each other out in the total mass flux balance. To further analyse the airflow at the eastern border, we show the average zonal and meridional wind ~~separately~~ in Fig. 9 for the *fire-run* (a & c). Additionally, we show the difference between the *fire-run* and the *ref-run* (b & d) to highlight the acceleration and deceleration of the horizontal winds due to the SCQ fire. Figure 9b reveals

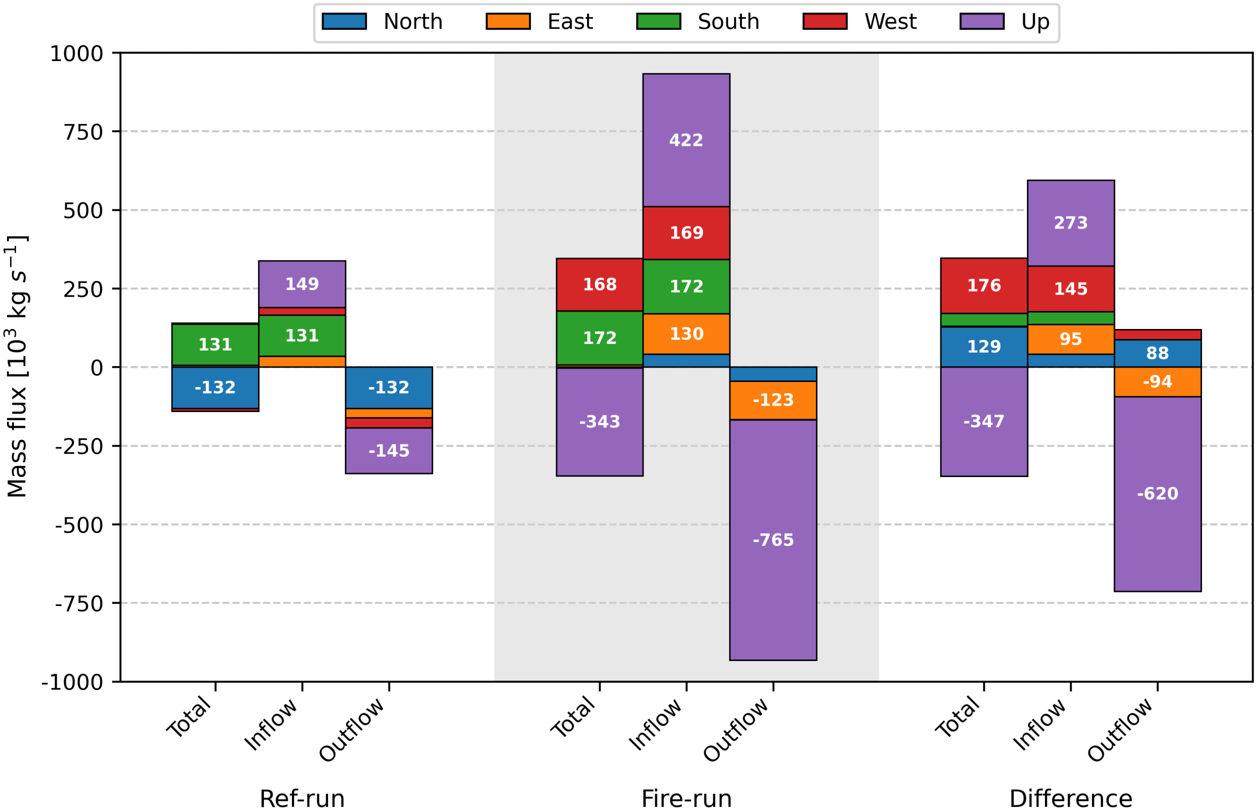

Figure 8. The mass flux balance for the *ref-run* and *fire-run* calculated over the boundaries of the red box in Fig. 7 in the lowest three layers of the simulation ($0 < z < 60$ m) between 19 and 20 UTC. The inflow (outflow) into the red box is defined as positive (negative). To investigate the impact of the SCQ fire on the mass transport, the difference between the two simulations (i.e., *fire-run* - *ref-run*) is shown.

two opposite changes at the eastern border: deceleration and acceleration of the zonal wind north and south of the centre of the fire (y = 12.8125 km; purple dash-dot line), respectively. ~~This~~ The combination of deceleration and acceleration explains the simultaneous increase in in- and outflow at the east border.

~~Although negligible for the net mass flux balance, the changes in the easterly in- and outflow affect the fire behaviour. Firstly, the additional inflow means an increase in oxygen supply for the fire, allowing for a higher combustion rate. In total, the SCQ fire increased the inflow by more than 170%, meaning that the time in which the air inside the red box is refreshed decreases from 2.3 minutes (*ref-run*) to 0.8 minutes (*fire-run*). Secondly, spot fires, which were observed during the SCQ fire, will experience different wind directions depending on their location ahead of the main fire and therefore behave differently. To illustrate the relevance, we consider a simplified scenario in which the wind is the primary factor in determining the direction of the fire spread. In this scenario, a spot fire at the northern part of the front would spread in the opposite direction of the main fire (black dotted outline), thereby reducing fuel availability ahead. On the other hand, at the southern part of the front, the spot~~

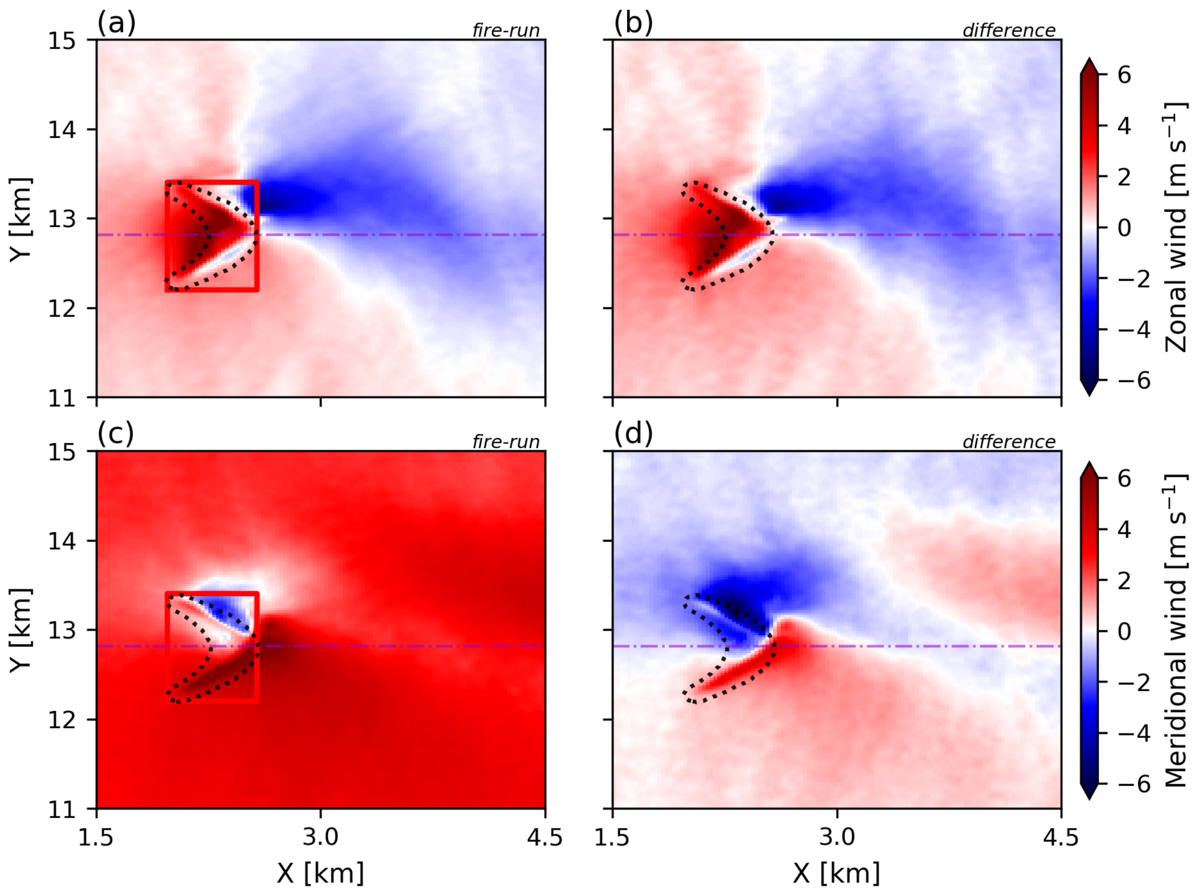

Figure 9. The average zonal **(a)** and meridional **(c)** wind between 19 and 20 UTC at the lowest vertical level of the simulation (z = 10 m). To visualise the acceleration and deceleration due to the SCQ fire, the average difference ~~with~~ between the *fire-run* and the *ref-run* is shown for both the zonal **(b)** and meridional **(d)** wind. The black dotted line and the purple dash-dot line indicate the simulated flaming zone of the SCQ fire (Fig. 2) and the centre of the fire (i.e. y=12.8125 km). The red rectangle shows the boundaries over which the mass flux balance in Fig. 8 is calculated.

~~fires would move in the same direction, enhancing the rate of spread. Besides affecting the behaviour of spot fires, the changed winds ahead of the main fires also affect the way backing fires can be used to reduce the fuel availability.~~

Figure 10 shows the evolution of the surface wind patterns with altitude (Figs. 7 ~~&~~ – 9). We limit ourselves to ~~vertical~~ average east-west cross-sections ~~parallel to the fire spread direction (i.e., eastward)~~ since the simulated plume also developed to the east. The southerly winds at the surface (Fig. 3d) would suggest otherwise, but the westerly winds above 500 m altitude (Fig. 3d) result in the plume developing towards the east, similar to the observations described in Sect. 2.1. Hence, the east-west cross-sections ~~parallel to the fire spread direction~~ are the most relevant for further analysis.

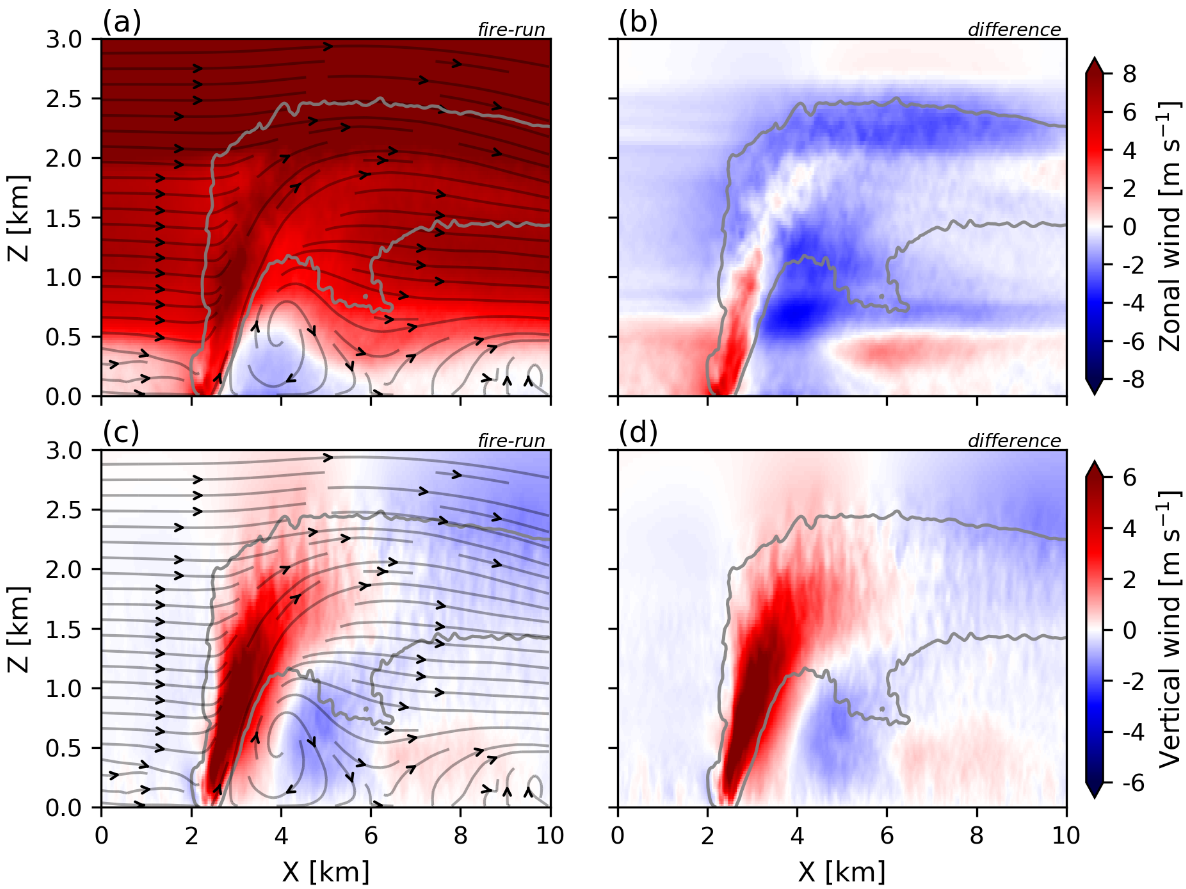

Figure 10. The vertical cross-sections of the average zonal **(a)** and vertical **(c)** wind between 19 and 20 UTC through the ~~middle~~ centre of the simulated fire (~~i.e. y = 12812.5 m~~purple dash-dot line; Fig. 9). The grey outline and grey streamlines represent the average plume shape based on the inert tracer and the airflow through the cross-section. To visualise the acceleration and deceleration of the wind due to the SCQ fire, the average difference ~~with~~ between the *fire-run* and the *ref-run* is shown for the zonal **(b)** and vertical **(d)** wind.

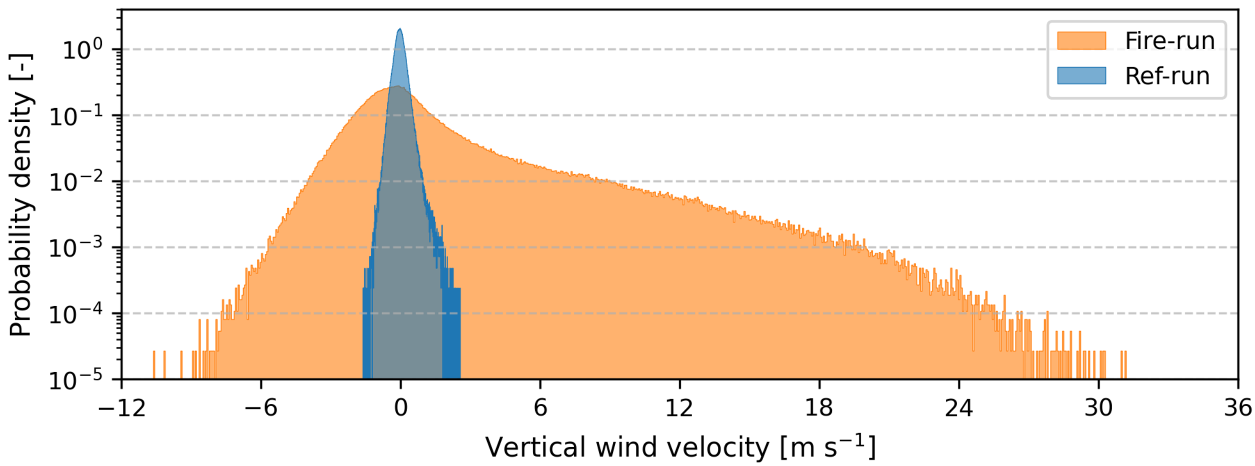

Figure 11. The probability density function of the instantaneous vertical wind inside the plume (grey outline in Fig. 10) between 19 and 20 UTC for both the *ref-run* (blue) and *fire-run* (orange).

While both the acceleration and deceleration areas of the zonal wind extend up to 1.5 km altitude, their patterns differ (Fig. 10b). The acceleration occurs primarily inside the plume (grey outline), with the maximum acceleration at the surface. In contrast, the deceleration mainly occurs to the east of the fire (from x = 2.6 km onward), with the maximum deceleration between 0.5 and 1 km altitude.

The largest impact on the vertical wind is the acceleration inside the plume (Fig. 10d), resulting in ~~instantaneous vertical wind speeds up to 32~~ average vertical velocities up to 6 m s^{-1} (~~not shown). Additionally,~~ Fig. 10c). We cannot directly compare the average simulated vertical velocities with instantaneous observations, which typically indicate vertical velocities of 10 to 30 m s^{-1} (Banta et al., 1992; Lareau and Clements, 2017; Clements et al., 2018). The temporal averaging in Fig. 10 ~~d shows the development of downdrafts ahead of the fire between x = 4 and 6 km up to 1.2 km altitude.~~ smooths away the instantaneous peaks in the simulated vertical velocities, resulting in relatively low average vertical velocities compared to instantaneous vertical velocities. In Fig. 11 we show the probability density function of the instantaneous vertical velocities inside the simulated plume (grey outline in Fig. 10) between 19 and 20 UTC for both the *ref-run* (blue) and *fire-run* (orange). When considering the instantaneous vertical velocities, we find updrafts up to 32 m s^{-1}, which matches the typical observed range of vertical velocities (Lareau and Clements, 2017; Clements et al., 2018). The same difference is visible between the average and instantaneous downdrafts. Averaged over time, the downdrafts peak at ±2 m s^{-1} (Fig. 10c), while Fig. 11 shows that instantaneous downdrafts have velocities up to 10 m s^{-1}.

The combined effect of these changes in the average zonal and vertical wind by the SCQ is visualised by the grey streamlines (Fig. 10a,c), which show the average airflow between 19 and 20 UTC. They reveal the formation of ~~a fire-induced circulation~~ downdrafts 2 km east of the ~~SCQ fire(x > 2.6 km) consisting of~~ fire, in addition to the rising motions inside the plume~~, downdrafts 2 km east of the fire and a~~ . Between the up- and downdrafts, a fire-induced circulation is visible, consisting of negative zonal wind near the surface (z < 0.5 km) and positive zonal wind aloft. Furthermore, ~~they~~ the streamlines show descending inflow west of the fire (x < 2 km) despite the relatively small negative average vertical velocities upwind compared to the downdrafts ahead of the fire (Fig. 10c).

Considering that the SCQ fire spread eastward in reality (Fig. 1), these modifications of the airflow suggest that the SCQ fire also altered the thermodynamic structure of the atmospheric boundary layer ahead of itself. Changing the thermodynamic structure could potentially improve its future burning conditions (i.e., temperature, moisture, and stability), thereby explaining the continued burning of the SCQ fire until midnight.

3.3 Fire-modified boundary layer

To analyse the impact of the fire-modified wind ~~patterns~~ (Fig. 7 to 10) on the thermodynamic structure of the atmospheric boundary layer, we show the average vertical cross-sections of the virtual potential temperature (θ_v) and specific humidity (q) during the *fire-run* in Fig. 12a,c. To highlight the impact of the SCQ fire on the thermodynamic structure, Fig. 12b,d shows the difference in θ_v and ~~q~~ q between the *fire-run* and the *ref-run*.

Inside the plume (grey outline), we observe heating near the surface (z < 1 km; Fig. 12b), while moistening only begins above 0.5 km (Fig. 12d). This indicates that the fire directly affects θ_v through the sensible heat flux, while q is primarily affected indirectly through the upward transport of ambient moisture by the fire-induced convection.

East of the plume (x > 2.6 km), two opposite patterns developed. Closest to the plume (2.6 < x < 4.5 km), Fig. 12b,d shows cooling and moistening in the lower part of the residual layer (0.5 < z < 1 km). Further eastward (4.5 < x < 8 km), the transition zone between the neutral boundary layer and the residual layer (0.25 < z < 0.75 km) is warmed and dried. These two opposite patterns reflect the interaction of the ~~fire-induced circulation~~ fire-modified winds with the ambient boundary layer structure ~~in which~~ surrounding the SCQ fire~~occurred~~. Between 19 and 20 UTC, there is a neutral boundary layer (0 < z < 0.5 km) topped by a warmer and drier residual layer (0.5 < z < 2 km), which in turn is topped by an even warmer and drier free troposphere (Fig. 3a,b). Closest to the plume (2.6 < x < 4.5 km), the fire-induced circulation transports relatively cool and moist air from the neutral boundary layer into the residual layer above. Further eastward (4 < x < 6 km), the downdrafts transport relatively warm and dry air downward from the residual layer to the neutral boundary layer. A similar pattern of warming and drying, albeit less strong, is present west of the plume due to the descending rear inflow.

To explore how the upward (downward) transport of relatively cold (warm) air (Fig. 12) affects the atmospheric boundary layer structure, we show the evolution of the average vertical profile of θ_v between 19 and 20 UTC as a function of the eastward distance (x_{ed}) from the fire (Fig. 13). Directly above the fire (x_{ed} = 0), the heating by the fire deepens the boundary layer from 0.5 km to 2 km (Fig. 13b). West of the fire (x_{ed} = -0.8 km), the descending inflow lowers the neutral boundary layer height (Fig. 13a). East of the fire, two ~~distinctly different~~ opposite effects associated with the ~~fire-induced circulation~~ fire-modified winds become apparent before the impact of the fire on the atmospheric boundary layer structure becomes negligible at x_{ed} = 7.5 km (Fig. 13e). Near the fire (x_{ed} = 1.5 km), upward transport of relatively cold air (Fig. ~~13~~12) leads to a deepening of the neutral boundary layer (Fig. 13c). Further eastward (x_{ed} = 3.5 km), the downdrafts (Fig. ~~7~~12) lower the boundary layer height (h) from 0.5 to 0.25 km (Fig. 13d).

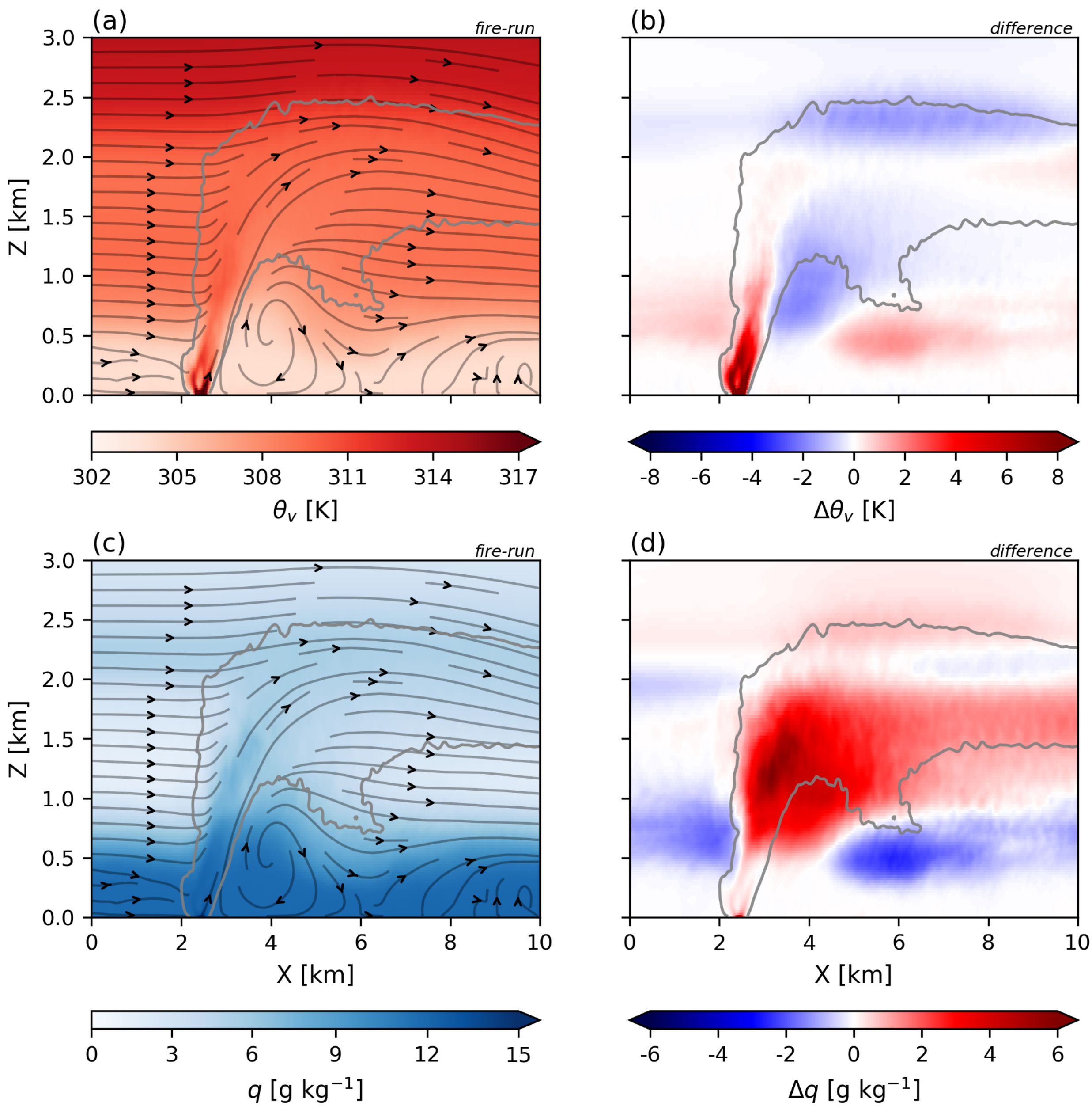

Figure 12. The vertical cross-sections of the average virtual potential temperature, θ_v **(a)**, and specific humidity, q **(c)**, between 19 and 20 UTC through the ~~middle~~ centre of the simulated fire (~~i.e. y = 12.8125 km~~purple dash-dot line; Fig. 9). To highlight the impact of the SCQ fire, the average difference ~~with~~ between the *fire-run* and the *ref-run* between 19 and 20 UTC is shown for θ_v **(b)** and q **(d)**. The grey outline visualises the average shape of the simulated plume. Furthermore, the grey streamlines indicate the airflow during the simulated SCQ fire.

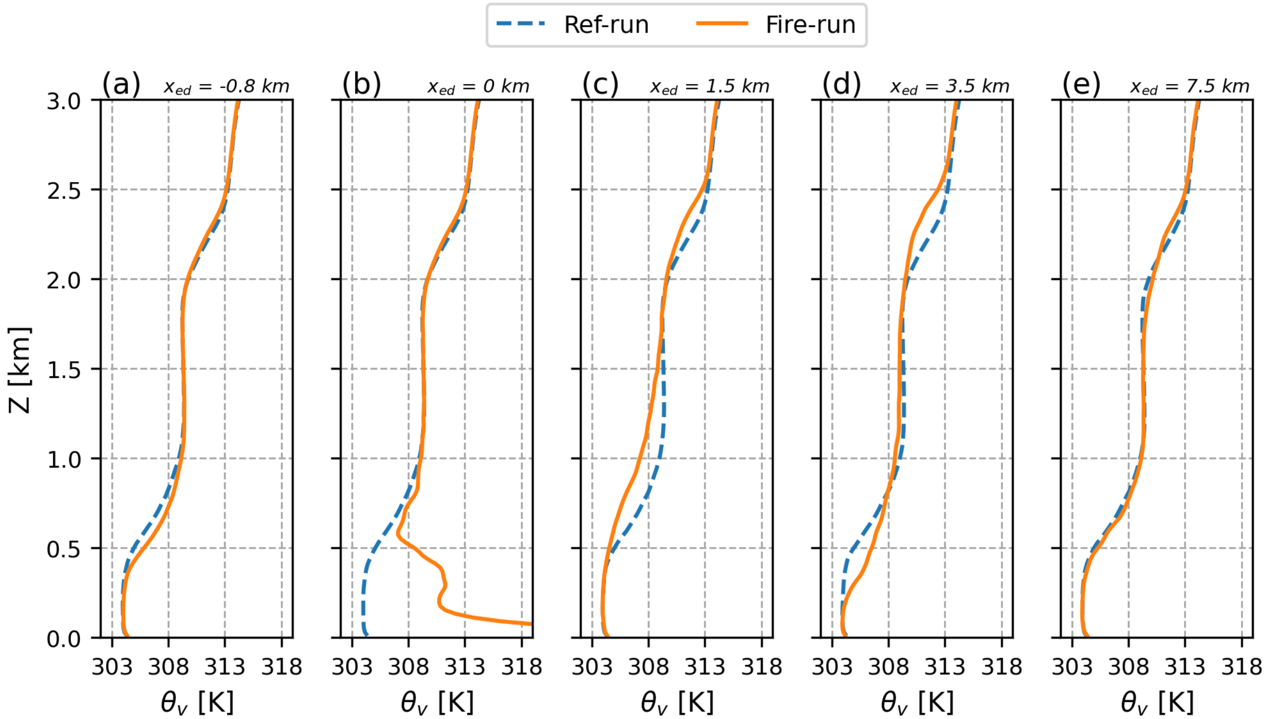

Figure 13. The average vertical profile of θ_v between 19 and 20 UTC for five eastward distances (x_{ed}) with respect to the head of the fire (x = 2.5 km, y = 12.8125 km): -0.8 km **(a)**, 0 km **(b)**, 1.5 km **(c)**, 3.5 km **(d)** and 7.5 km **(e)**. These five locations are visualised in Fig. 14a with red hexagons. To show the impact of the SCQ fire on ~~that~~ the thermodynamic structure of the atmospheric boundary layer~~structure~~, the vertical profiles of θ_v for both the ~~simulation with (orange)~~ *fire-run* and ~~without (blue dotted) a fire~~ *ref-run* are shown.

To investigate the spatial extent of these changes in h, we calculated h based on the minimum $\frac{dq}{dz}$ between 0.1 and 1.6 km altitude (Fig. 14). ~~This~~ The gradient in q identifies the interface between the relatively moist neutral layer and the drier residual layer (Fig. 3b), consistent with the mixed-layer framework described by Vilà-Guerau De Arellano et al. (2015). The altitude range is chosen to exclude the surface layer (z < 0.1 km) and the capping inversion on top of the residual layer (2 < z < 2.5 km). We find a decrease in h at the rear of the flaming zone, matching the descending rear inflow (Fig. 12). A similar decrease in h is visible at the northern and southern flanks of the SCQ fire, suggesting that a similar descending inflow is present at the flanks. Ahead of the flaming zone (black dotted line), we find the same pattern as in Fig. 12 with an increase in h within the first 2 to 3 km and subsequently a decrease in h. Figure 14b shows that both the increase and decrease in h are advected towards the southeast by the airflow above the convective boundary layer (black streamlines). The southeast advection explains why we find no modification of the thermodynamic structure at 7.5 km ahead of the fire (Fig. 13e). This lack of modification highlights the significance of directional wind shear in determining where and how far ahead of itself a fire can alter the thermodynamic structure of the atmosphere. In case of the SCQ fire, the wind veered from a southerly surface

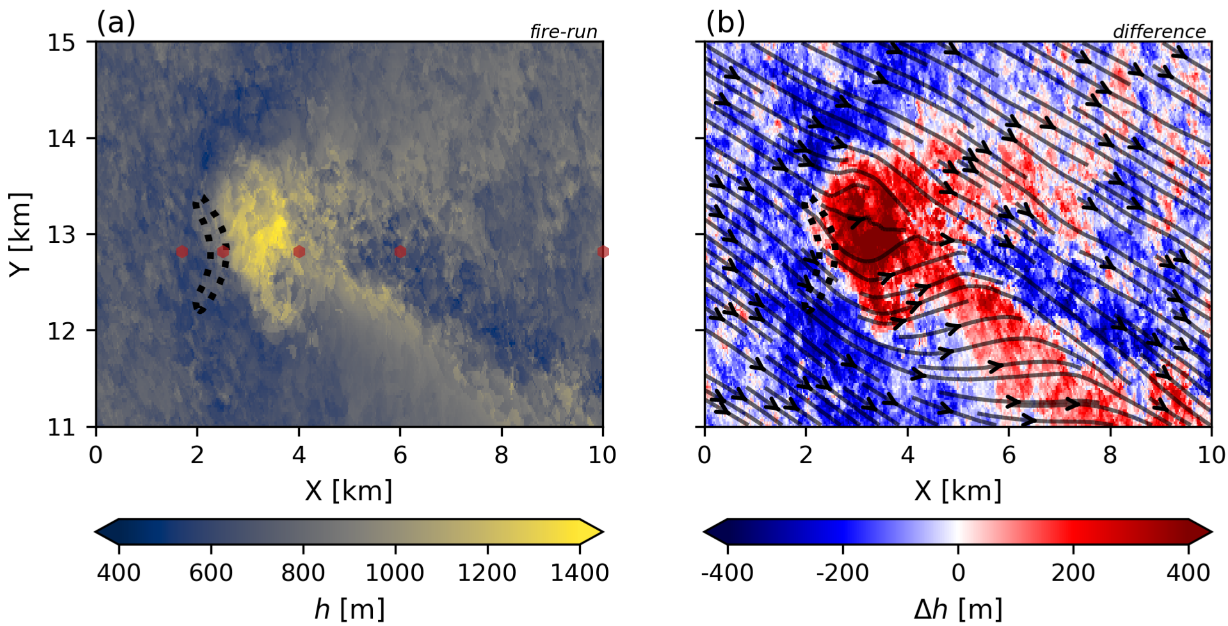

Figure 14. The average boundary layer height, h **(a)** between 19 and 20 UTC based on the minimum $\frac{dq}{dz}$ between 0.1 and 1.6 km altitude. The red hexagons from left to right represent the locations of the vertical profiles **(a)** to **(e)** in Fig. 13. To highlight the impact of the SCQ fire on h, we calculated the difference in h between the *fire-run* and *ref-run* **(b)**. The black streamlines represent the average airflow in the residual layer based on the simulated airflow at 950 m altitude.

wind into a westerly to northwesterly wind above the boundary layer. Consequently, the change in h was advected towards the southeast, but with less (more) veering of the wind over height, the distance ahead of the SCQ fire with a modified h would be larger (smaller).

Besides affecting h, Fig. 13c & d shows that the SCQ fire also causes entrainment of free tropospheric air at the top of the residual layer (2 < z < 2.5 km). Comparing the vertical profiles at x_{ed} = 1.5 and 3.5 km reveals an increasing amount of entrainment with increasing eastward distance from the fire. This is because the plume is tilted, which means that the overshooting is tilted. Hence, the entrainment at the top of the residual layer is shifted in the direction of the wind, i.e. eastward in the case of the SCQ fire.

4 Discussion

In this study, we demonstrated the use of an in-plume sounding ~~measurements to explicitly validate~~ to explicitly evaluate an LES of the pyro-convection induced by the SCQ fire. Using the ~~validated~~ LES, we investigated the impact of pyro-convection on the wind patterns and subsequently the thermodynamic structure of the atmospheric boundary layer surrounding the SCQ fire. In this chapter, we reflect on our results and methodology in comparison to previous work and outline implications for future research.

4.1 Fire-modified wind patterns

Figure 15b summarises the key impacts of pyro-convection on the surrounding wind patterns found in our simulation of the SCQ fire (Fig. 9 to 12and 10). The convection inside the plume (1) created an accelerated descending rear inflow (2) and the formation of a circulation ahead of the fire consisting of the rising plume (1), downdrafts two km downdrafts ahead of the fire (3) and frontal inflow with a fire-induced circulation in between (4).

The acceleration of the rear inflow (2) in our simulation aligns with previous studies (Coen et al., 2013; Peace et al., 2016; Filippi et al., 2018) and confirms the theory proposed by Potter (2012a, b) that the upward mass flux due to pyro-convection accelerates the rear inflow (Fig. 15a). As discussed in the introduction, this theory provides a plausible explanation for the faster-than-predicted fire spread observed for extreme wildfire events that trigger pyro-convection. Current operational fire spread models do not account for the accelerated rear inflow due to pyro-convection (Kochanski et al., 2013). Hence, the wind experienced by the fire is underestimated by these models, which results in an underestimation of the fire spread. Recent in-plume measurements (Castellnou et al., 2022) confirmed this theory by showing a positive correlation between the

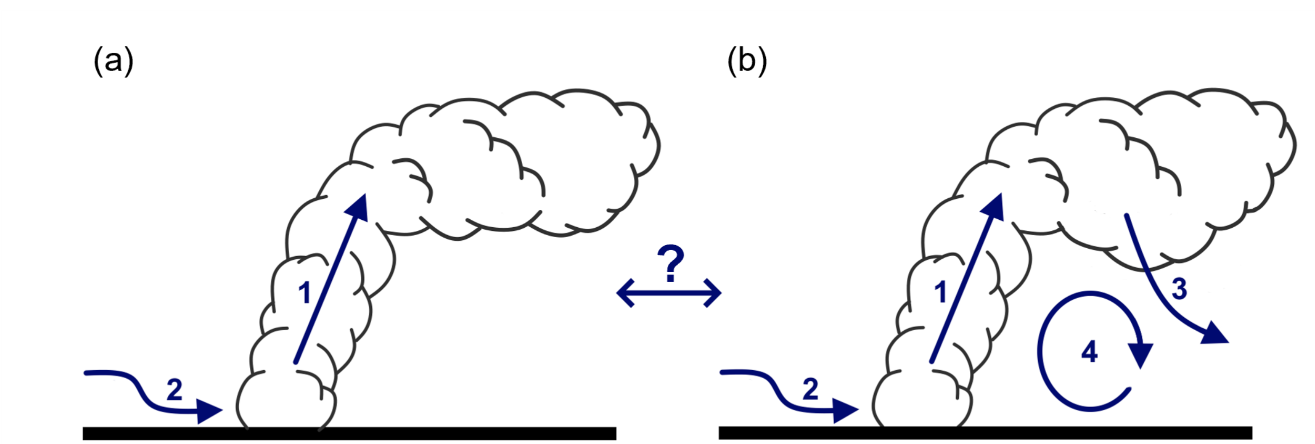

Figure 15. **(a)** A schematic overview of the impacts of pyro-convection on the wind patterns following Potter (2012a, b): (1) convective motions inside the plume and (2) accelerated and descending rear inflow. **(b)** An extended version of **(a)** including the fire-induced circulation, which consists downdrafts ahead of the fire (13) convective motions inside and the plume, fire-induced circulation (34) downdrafts ahead of in between the fire up- (1) and downdrafts (43)frontal inflow. The extended schematic is based upon the outcomes of the SCQ fire simulations (Fig. 79 and 10) combined with previous observations (Banta et al., 1992; Roberts et al., 2024) (Banta et al., 1992; Lareau and Clements, 2017; Roberts et al., 2024) and simulations (Sun et al., 2009; Coen et al., 2013; Peace et al., 2016). The question mark highlights the unknown factors that govern the development of the fire-induced circulationscirculation, as they do it is not appear found in all previous studies (e.g. Filippi et al., 2018).

pyro-convective strength and the mismatch between predicted and observed fire spread; The stronger the pyro-convection, the stronger the In addition to the acceleration of the rear inflow, which means a larger underestimation we also find fire-modified wind patterns ahead of the fire spread by the operational models (i.e. larger mismatch between predictions and observations).

However, our results suggest that this explanation for the mismatch between predicted and observed fire behaviour is incomplete. In addition to the acceleration of the rear inflow described by Potter (Fig. 15a) , we find the development of (Fig. 15b). The results show the development of downdrafts 2 to 3 km ahead of the fire (3) and a fire-induced circulation ahead of the fire (Fig. 15b) (4) in between the convective plume (1) and the downdrafts (3). The existence of such a fire-induced circulation has been (in)directly suggested in previous studies. Based on Doppler measurements of the horizontal wind, Banta et al. (1992) suggested the presence of a circulation ahead of the fire, which, similarly to our results, was observed in between the convective plume and downdrafts 2 to 3 km ahead of the fire. Furthermore, both observations (Roberts et al., 2024) and our simulations and the observations by Banta et al. (1992) show that the downdrafts are directed away from the fire and thus away from the circulation.

Other observations (Lareau and Clements, 2017; Roberts et al., 2024) and simulations (Sun et al., 2009; Coen et al., 2013; Peace et al., 2016) show do not explicitly show a fire-induced circulation, but they do show the development of frontal inflow, suggesting the presence of a fire-induced circulation. Coen et al. (2013) suggested that the frontal inflow can alter the fire behaviour by counteracting the acceleration of the rear inflow . AdditionallySimultaneously, we recognise that frontal inflow does not appear in all previous studies (e.g. Filippi et al., 2018). In our simulation of the SCQ fire, the frontal inflow also shows spatial variability, occurring predominantly in the northern section of the front (Fig. 9). This variability is physically and operationally relevant, as the frontal inflow is a known indicator for extreme wildfire behaviour. Specifically, radar observations indicate that frontal inflow is linked to the formation of fire-generated vortices (Lareau et al., 2022). This matches operational observations , which suggest aligns with operational observations by the Catalan Fire and Rescue Service, which indicate that frontal inflow is typically associated with the occurrence of fire-generated vortices and long-range spot fires, two phenomena that were also observed during the SCQ fire. Therefore, based on our findings combined with the previous observations (Banta et al., 1992; Lareau et al., 2022; Roberts et al., 2024), simulations (Sun et al., 2009; Coen et al., 2013; Peace et al., 2016) and operational observations, we propose to extend the theory provided by Potter (2012a, b) to include the . Despite the relevance of the frontal inflow, the drivers of the frontal inflow, and thus the fire-induced circulation (Fig. 15) to explain the mismatch between observed and predicted fire behaviour.

Simultaneously, we recognise that frontal inflowdoes not appear in all previous studies (e.g. Filippi et al., 2018). Furthermore, in our simulation of the SCQ fire, the frontal inflowalso shows spatial variability, occurring predominantly in the northern section of the front (Fig. 9). Hence, to further understand the influence of pyro-convection on fire behaviour, we need to know circulation, remain unknown. Hence, further research is necessary to investigate under which conditions (extreme) wildfire events can create frontal inflow and subsequently how the changes in airflow at the rear and in front of the fire affect the fire behavioura fire-induced circulation and to verify the observed connection to long-range spotting.

4.2 Fire-modified boundary layer

We studied the impact of the fire-modified winds (Fig. 15) on the surrounding thermodynamic structure of the atmospheric boundary layer to investigate whether the SCQ fire counteracted the cooling, moistening and stabilisation of the atmosphere at night ahead of itself. When possible, these changes could explain the continued burning throughout the night of the SCQ fire. We found no warming or drying of the atmosphere at the surface due to the descending motions (Fig. 12). However, we did find two opposite changes in the boundary layer structure ahead of the fire (Fig.13). Within the first 2 km ahead of the fire, we found a 40 to 60% deepening of the neutral boundary layer. Further ahead, between 2 and 4 km ahead of the fire, we observed a 50% decrease in boundary layer height.

Although the boundary layer height is not directly linked to fire behaviour, it is connected to plume growth. Generally, a higher well-mixed boundary layer is beneficial to plume growth. This suggests that when a fire, such as the SCQ fire, increases the boundary layer height ahead, it makes it easier for a fire to maintain a convective plume while advancing. We know from observations (e.g. Castellnou et al., 2022), that pyro-convection generally increases fire spread rates. Hence, we hypothesise that by modifying the boundary layer ahead, a fire can more easily sustain a convective plume, which would then promote continued burning throughout the night, despite worsening burning conditions (i.e., cooling and moistening). The opposite applies when the boundary layer height is decreased; in that case, it becomes harder to sustain a convective plume, which is expected to decrease the ability of a fire to continue burning throughout the night.

This hypothesised impact on the fire behaviour only applies to fires that spread in the same direction as their plume, since that is the region where the boundary layer is modified. Hence, the hypothesis applies to the SCQ fire, since both the fire and plume spread eastward, which corresponds with the area where the boundary layer structure was modified in the simulation (Fig. 14). Visual observations suggest that the hypothesis is a plausible explanation for the continued burning until midnight by the SCQ fire, as the fire not only burned until midnight (22 UTC) but also maintained a convective plume throughout the night (Fig. 1a). With this explanation, we assume that the SCQ fire ~~continually deepens~~ would continually deepen the boundary layer ahead ~~as it advances~~ while advancing forward.

A further complicating factor for predicting the impact of the ~~modified boundary layer structure~~ fire-modified boundary layer on the fire behaviour is the formation of a surface inversion throughout the night. The surface inversion is not yet present in this case study as we focus on the period (19–20 UTC) surrounding the shift from a positive to a negative surface heat flux (19:41 UTC). Consequently, there has been insufficient time for the formation of a surface inversion in this case study. We expect that the formation of a surface inversion in the ~~environment~~ surroundings of the SCQ fire would limit the ability of the fire to maintain a convective plume and subsequently limit the extent to which the pyro-convection can alter the thermodynamic structure of the atmosphere ahead of the fire. Simultaneously, it is unknown how the ~~fire-induced circulation~~ fire-modified winds would affect the surface inversion ahead of the fire. Hence, to test the hypothesis, further studies using a two-way fire atmosphere coupling are needed to investigate the extent to which a modified boundary layer structure explains continued nighttime burning, for example, during the SCQ fire.

4.3 Strengths and limitations of in-plume sounding measurementssoundings

We specifically chose the SCQ fire as a case study for its availability of both fire-behaviour observations and pyro-convection measurements (CFRS, 2022; Castellnou et al., 2022). For this fire, an in-plume soundings were radiosonde was released that measured the thermodynamic structure (θ_v, q) inside the plume and the environment during their ambient conditions during its ascent and descent, respectively. The ability to validate the environment in which the plume was simulated was essential to our validation. The validation availability of measurements of the ambient conditions was essential for understanding the differences between the observations and the simulation. The comparison with observations revealed an overestimation of the simulated inversion height. Using the environmental measurements of the sounding, we could identify ambient conditions, we identified the underlying cause of the overestimation.

Simultaneously, we recognise the limitations of sounding measurementssoundings. It is impossible to control the exact measurement locations as the path of the soundings radiosonde is controlled by the ambient and in-plume turbulent structures. Furthermore, the spatial and temporal extent of the sounding measurements is limited to a single timeseries and a single measurement per altitude. Lastly, the soundings radiosondes are intended for atmospheric measurements, which means that so they do not provide quantitative measurements of the fire behaviour.

Other tools, such as Doppler radars (e.g. Banta et al., 1992; Clements et al., 2018; Roberts et al., 2024) and Unmanned Aerial Vehicles (UAVs; Kiefer et al., 2012; Bailon-Ruiz et al., 2022), would therefore complement the sounding radiosonde measurements. UAVs can be used for in-plume measurements of temperature and moisture, similar to soundings, but when equipped with infrared sensors, they can also measure fire behaviour. Doppler radars measure the kinematic plume structure, which complements the sounding radiosonde measurements of θ and q. Besides the complementary measurements, depending on their usage, both the Doppler radar and the UAVs provide offer a larger spatial and/or temporal coveragecoverage, higher temporal resolution, or a combination of both. Hence, under ideal circumstances, these tools are combined to get a complete set of measurements capturing wildfire-atmosphere interactions: the thermodynamic plume structure (soundings), the kinematic plume structure (Doppler radars) and the fire behaviour (UAVs).

However, Doppler radars and UAVs are relatively expensive and complex to operate compared to soundingsradiosondes. Consequently, Doppler radars and UAVs are primarily used in dedicated campaigns, whereas the accessibility of the soundings radiosondes allows for operational usage by firefighters (Castellnou Ribau et al., 2025). The operational usage means that soundings the radiosonde measurements have the potential to capture a broader range of wildfire-induced plumes, inherently also capturing a wider variety of meteorological conditions. Therefore, we find that soundings in-plume radiosondes offer a baseline opportunity for validating evaluating (large-eddy) simulations of pyro-convection. When feasible, we recommend complementing these measurements with additional tools that capture the kinematic plume structure and fire behaviour, such as Doppler radars and UAVs, to extend the validation evaluation possibilities.

4.4 Implications for future research

To address the open questions raised in the discussion above, a different methodology is required compared to this case study. In this case study, we chose to implement the SCQ fire as a stationairy area of elevated heat and moisture fluxes. This simplification of the fire behaviour enabled us to use temporal averages to determine whether the fire consistently modified the surrounding wind (e.g. Fig. 10), θ and q fields (e.g. Fig. 12). Although this simplification allowed for a focus on the impact of the SCQ fire on the atmosphere, the goal of this case study, it inhibits further study into the effects of the altered atmosphere on the fire spread.

Simultaneously, we used ERA5 boundary conditions to recreate the meteorological conditions of the SCQ fire as realistically as possible to ensure a realistic impact of the simulated fire on the atmosphere. The downside of atmospheric realism is that the meteorological processes, such as advection and surface fluxes, change simultaneously and continuously over time, making it impossible to isolate the processes governing the ~~wildfire-atmosphere interactions~~impact of pyro-convection on the surrounding atmosphere. Consequently, identifying the conditions needed for a fire to create a fire-induced circulation ahead of itself is impossible with the simulation setup of this case study.

Hence, future work could take two opposite directions: either increasing model complexity by including a two-way coupled fire spread model or decreasing complexity by using idealised meteorological conditions. The first pathway enables further understanding of how ~~the modified~~ a fire-modified atmosphere affects the fire spread behaviour (e.g. Sun et al., 2009). In contrast, the second is focused on controlling all parameters of the simulation to isolate the processes governing ~~wildfire-atmosphere interactions~~the impact of pyro-convection on the surrounding atmosphere (e.g. Cunningham et al., 2005). Our future work will follow the second path, ~~where we will focus~~ focusing on systematically quantifying and subsequently parameterising the change in rear and frontal inflow. With this parameterisation, we aim to include the effects of pyro-convection on the surface winds in operational fire spread models.

5 Conclusions

The objective of this study was threefold: (1) replicate the measured in-situ thermodynamic structure of wildfire plumes using LES; (2) study the proposed impact of pyro-convection on the surrounding wind patterns by previous studies; and (3) analyse the impact of the ~~fire-driven~~ fire-modified wind patterns on the thermodynamic structure of the atmospheric boundary layer.

The comparison with visual observations and an in-plume sounding ~~measurements~~ of the SCQ fire showed that MicroHH is a suitable tool for studying the impacts of pyro-convection on the surrounding kinematic and thermodynamic structure of the atmosphere. The simulated plume shape and in-plume θ_v matched the observations. The main discrepancy was the overestimation of the ambient atmospheric boundary layer height by ~~0.4 km, but this~~ 0.3 km, which was caused by the ERA5 boundary conditions and does not reflect the performance of MicroHH.

The in-depth analysis of the wind patterns revealed that pyro-convection accelerates the rear inflow~~, matching the hypothesised primary impact of pyro-convection on the surrounding airflow. However, we also~~. Additionally, we found the formation of a fire-induced circulation ahead of the SCQ fire ~~, which consists of~~ between the convection within the plume ~~, downdrafts~~ and downdrafts 2 km ahead of the fire~~, and frontal inflow into the fire. We argue that there are two pathways through which the fire-induced circulation can affect the fire behaviour. Firstly, the frontal inflow could counter the accelerated rear inflow, and its presence is associated with the occurrence of fire-generated vortices and long-range spotting. Secondly, we found that the fire-induced circulation modifies the~~ . These fire-modified winds ahead of the fire subsequently altered the thermodynamic structure of the ~~boundary layer~~ atmospheric boundary layer, causing it to deepen for 2 km ahead of the fire~~. The circulation causes simultaneous deepening and thinning of the boundary layer in the 4 km ahead, thereby disrupting the transition from the convective daytime to a stably stratified nighttime boundary layer. This disruption provides a plausible explanation for the sustained nighttime burning during the SCQ fire. Therefore, we argue that the primary impact of pyro-convection on wildfire behaviour depends on the combined effect of changes in wind patterns at the rear and in front of the fire (revised hypothesis), rather than solely on the acceleration of the rear inflow (original hypothesis~~, followed by 2 km of thinning.

Hence, the hypothesis that the fire-modified winds would lead to heating and drying of the air near the surface is rejected. Instead, we found that the fire-modified winds, specifically the fire-induced circulation, changed the thermodynamic structure of the atmospheric boundary layer at higher altitudes (> 0.25 km).

Code and data availability. The sounding data and the synoptic weather station data for the SCQ fire are published by Ribau et al. (2022). The simulation settings, along with the surface boundary conditions, are available at https://doi.org/10.5281/zenodo.17159896. This repository also includes the fire perimeter shown in Fig. 1.

Appendix A: Validation of the periodic boundary conditions based on the specific humidity

~~We used periodic boundary conditions for the simulations with MicroHH, allowing air recirculation throughout the domain.It is a commonly used technique to simulate convective boundary layers with turbulence-resolving large-eddy simulation tools such as MicroHH. However, when adding a fire as a source of heat and moisture, we risk that the moisture and heat released by the fire circulate through the~~ In Fig. A1 we show the vertical profiles of the specific humidity (q) at each of the four borders of the simulated domain for both the *ref-run* (blue dashed line) and *fire-run* (orange line). There is no significant difference between the two profiles at any of the four borders of the domain, indicating the domain ~~, subsequently modifying the thermodynamic environment in which the plume develops. To prevent this unrealistic impact on the thermodynamic environment of the plume, we extended the domaineastward. Figures **??** and **??** confirm that the extended domain prevents this unrealistic behaviour. At all four borders, the vertical profiles of the virtual potential temperature and specific humidity do not significantly differ between the simulations with (i.e. fire-run) and without (i.e. ref-run) a fire . Hence, the periodic boundary conditions do not significantly impact the results of this study~~is sufficiently large in terms of q, to prevent any recirculation of the moisture released by the simulated fire in the *fire-run*.

~~The same as in Fig. **??**, but for q instead of θ_v.~~

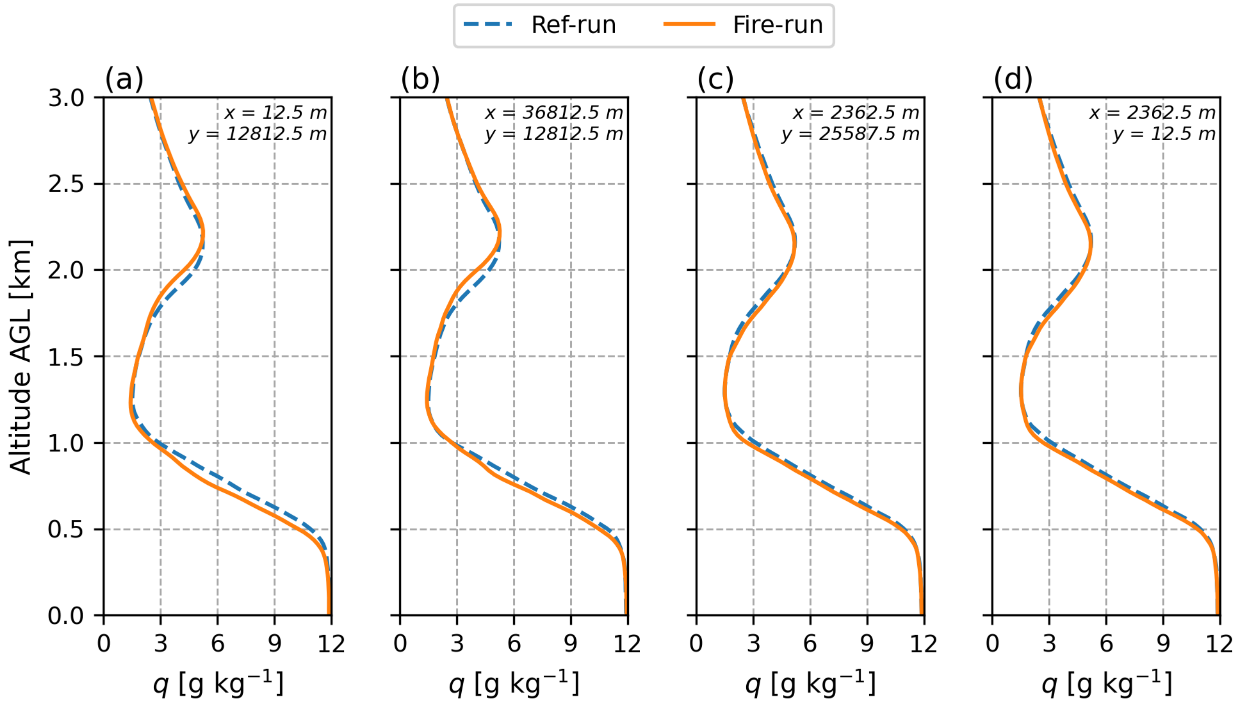

Figure A1. The ~~averaged vertical profiles of θ_v between 19 and 20 UTC for the simulation without (ref-run) and with fire (fire-run) at the four borders of the domain: western **(a)**, eastern **(b)**, northern **(c)**, and southern **(d)**. The x and y values indicate the exact location of the vertical profiles following the coordinate system shown~~ same as in Fig. ~~2~~4, but for q instead of θ_v.

Author contributions. TR performed the LES simulations and subsequent analysis and wrote the paper. CH set up the initial setup of the simulations and provided regular feedback on the ongoing analysis and paper writing. All authors assisted with the conceptualisation of the research and acted as internal reviewers.

Competing interests. The authors declare that they have no conflict of interest.

Acknowledgements. We thank the reviewers for their valuable suggestions. This project received funding from the Union Civil Protection Mechanism of the European Union under grant agreement No 101140363 (EWED). Hence, this project is funded by the European Union. Views and opinions expressed are however those of the authors only and do not necessarily reflect those of the European Union or the European Commission-EU. Neither the European Union nor the granting authority can be held responsible for them. Furthermore, we acknowledge the use of AI for coding suggestions (GitHub Co-Pilot) and grammar checking (Grammarly).

References

Bailon-Ruiz, R., Bit-Monnot, A., and Lacroix, S.: Real-Time Wildfire Monitoring with a Fleet of UAVs, Robotics and Autonomous Systems, 152, 104 071, https://doi.org/10.1016/j.robot.2022.104071, 2022.

Banta, R. M., Olivier, L. D., Holloway, E. T., Kropfli, R. A., Bartram, B. W., Cupp, R. E., and Post, M. J.: Smoke-Column Observations from Two Forest Fires Using Doppler Lidar and Doppler Radar, Journal of Applied Meteorology and Climatology, 31, 1328–1349, https://doi.org/10.1175/1520-0450(1992)031<1328:SCOFTF>2.0.CO;2, 1992.

Byram, G. M.: Atmospheric Conditions Related to Blowup Fires, NC: USDA-Forest Service. Southeastern Forest Experiment Station, Asheville, 36 pp., Station Paper SE–SP–35, 1954.

Byram, G. M.: Combustion of Forest Fuels, in: Forest Fire: Control and Use, edited by K. P. Davis, pp. 61–89, McGraw-Hill, New York, 1959.

Campos, C., Couto, F. T., Filippi, J.-B., Baggio, R., and Salgado, R.: Modelling Pyro-Convection Phenomenon during a Mega-Fire Event in Portugal, Atmospheric Research, 290, 106 776, https://doi.org/10.1016/j.atmosres.2023.106776, 2023.

Castellnou, M., Bachfisher, M., Miralles, M., Ruiz, B., Stoof, C. R., and de Arellano, J. V.-G.: Pyroconvection Classificatin Based on Atmospheric Vertical Profiling Correlation with Extreme Fire Spread Observations, Journal of Geophysical Research: Atmospheres, 127, e2022JD036 920, https://doi.org/10.1029/2022JD036920, 2022.

Castellnou Ribau, M., Bachfischer, M., Guarque, P., Estivill, L., Miralles Bover, M., Ruiz, B., Pagès, J., Verhoeven, B., Ntasiou, Z., Stokkeland, O., van Heerwaarden, C., Roelofs, T., Janssens, M., Stoof, C. R., and Vilà-Guerau de Arellano, J.: Integrating Fireline Observations to Characterize Fire Plumes during Pyroconvective Extreme Wildfire Events: Implications for Firefighter Safety and Plume Modeling, Atmospheric Measurement Techniques, 18, 7805–7831, https://doi.org/10.5194/amt-18-7805-2025, 2025.

CFRS: Fire Information Sheet: Santa Coloma de Queralt, Tech. rep., Catalan Fire Rescue Service (GRAF unit), 2022.

Clements, C. B., Lareau, N. P., Kingsmill, D. E., Bowers, C. L., Camacho, C. P., Bagley, R., and Davis, B.: The Rapid Deployments to Wildfires Experiment (RaDFIRE): Observations from the Fire Zone, Bulletin of the American Meteorological Society, 99, 2539–2559, https://doi.org/10.1175/BAMS-D-17-0230.1, 2018.

Coen, J. L., Cameron, M., Michalakes, J., Patton, E. G., Riggan, P. J., and Yedinak, K. M.: WRF-Fire: Coupled Weather–Wildland Fire Modeling with the Weather Research and Forecasting Model, Journal of Applied Meteorology and Climatology, 52, 16–38, https://doi.org/10.1175/JAMC-D-12-023.1, 2013.

Commissão Téchnica Independente: Análise e Apuramento Dos Factos Relativos Aos Incêndios Que Ocorreram Em Pedrogão Grande, Castanheira de Pera, Ansião, Alvaiázere, Figueiró Dos Vinhos, Arganil, Góis, Penela, Pampilhose Da Serra, Oleiros e Sertã, Entre 17 e 24 de Junho de 2017., Tech. rep., Assembleia Da Republica, 2017.

Couto, F. T., Filippi, J.-B., Baggio, R., Campos, C., and Salgado, R.: Triggering Pyro-Convection in a High-Resolution Coupled Fire–Atmosphere Simulation, Fire, 7, 92, https://doi.org/10.3390/fire7030092, 2024a.

Couto, F. T., Filippi, J.-B., Baggio, R., Campos, C., and Salgado, R.: Numerical Investigation of the Pedrógão Grande Pyrocumulonimbus Using a Fire to Atmosphere Coupled Model, Atmospheric Research, 299, 107 223, https://doi.org/10.1016/j.atmosres.2024.107223, 2024b.

Cunningham, P., Goodrick, S. L., Hussaini, M. Y., and Linn, R. R.: Coherent Vortical Structures in Numerical Simulations of Buoyant Plumes from Wildland Fires, International Journal of Wildland Fire, 14, 61–75, https://doi.org/10.1071/WF04044, 2005.

Davis, K. P.: Forest Fire: Control and Use, McGraw-Hill, New York, 1st edition edn., 1959.

Duane, A., Castellnou, M., Bachfisher, M., and Brotons, L.: Fire Rate of Spread and Growth Rate in a Set of 30 Global Wildfires: New Evidence of Extreme Fire Behavior, JOURNAL OF ENVIRONMENTAL INFORMATICS, 44, 87–99, https://doi.org/10.3808/jei.202400526, 2024.

Filippi, J.-B., Bosseur, F., Mari, C., and Lac, C.: Simulation of a Large Wildfire in a Coupled Fire-Atmosphere Model, Atmosphere, 9, 218, https://doi.org/10.3390/atmos9060218, 2018.

Finney, M. A., McAllister, S., Grumstrup, T. P., and Forthofer, J. M.: Wildland Fire Behaviour Dynamics, Principles and Processes, CSIRO Publishing, Clayton South, VIC, ISBN 978-1-4863-0910-8 978-1-4863-0909-2, 2021.

Gualtieri, G.: Reliability of ERA5 Reanalysis Data for Wind Resource Assessment: A Comparison against Tall Towers, Energies, 14, https://doi.org/10.3390/en14144169, 2021.

Hersbach, H., Bell, B., Berrisford, P., Hirahara, S., Horányi, A., Muñoz-Sabater, J., Nicolas, J., Peubey, C., Radu, R., Schepers, D., Simmons, A., Soci, C., Abdalla, S., Abellan, X., Balsamo, G., Bechtold, P., Biavati, G., Bidlot, J., Bonavita, M., De Chiara, G., Dahlgren, P., Dee, D., Diamantakis, M., Dragani, R., Flemming, J., Forbes, R., Fuentes, M., Geer, A., Haimberger, L., Healy, S., Hogan, R. J., Hólm, E., Janisková, M., Keeley, S., Laloyaux, P., Lopez, P., Lupu, C., Radnoti, G., de Rosnay, P., Rozum, I., Vamborg, F., Villaume, S., and Thépaut, J.-N.: The ERA5 Global Reanalysis, Quarterly Journal of the Royal Meteorological Society, 146, 1999–2049, https://doi.org/10.1002/qj.3803, 2020.

Kiefer, C. M., Clements, C. B., and Potter, B. E.: Application of a Mini Unmanned Aircraft System for In Situ Monitoring of Fire Plume Thermodynamic Properties, Journal of Atmospheric and Oceanic Technology, 29, 309–315, https://doi.org/10.1175/JTECH-D-11-00112.1, 2012.

Kochanski, A. K., Jenkins, M. A., Mandel, J., Beezley, J. D., and Krueger, S. K.: Real Time Simulation of 2007 Santa Ana Fires, Forest Ecology and Management, 294, 136–149, https://doi.org/10.1016/j.foreco.2012.12.014, 2013.

Lareau, N. P. and Clements, C. B.: Environmental Controls on Pyrocumulus and Pyrocumulonimbus Initiation and Development, Atmospheric Chemistry and Physics, 16, 4005–4022, https://doi.org/10.5194/ACP-16-4005-2016, 2016.

Lareau, N. P. and Clements, C. B.: The Mean and Turbulent Properties of a Wildfire Convective Plume, Journal of Applied Meteorology and Climatology, 56, 2289–2299, https://doi.org/10.1175/JAMC-D-16-0384.1, 2017.

Lareau, N. P., Nauslar, N. J., Bentley, E., Roberts, M., Emmerson, S., Brong, B., Mehle, M., and Wallman, J.: Fire-Generated Tornadic Vortices, Bulletin of the American Meteorological Society, 103, 1296–1320, https://doi.org/10.1175/BAMS-D-21-0199.1, 2022.

Mangan, M. R., Hartogensis, O., Boone, A., Branch, O., Canut, G., Cuxart, J., de Boer, H. J., Le Page, M., Martínez-Villagrasa, D., Miró, J. R., Price, J., and Vilà-Guerau de Arellano, J.: The Surface-Boundary Layer Connection across Spatial Scales of Irrigation-Driven Thermal Heterogeneity: An Integrated Data and Modeling Study of the LIAISE Field Campaign, Agricultural and Forest Meteorology, 335, 109 452, https://doi.org/10.1016/j.agrformet.2023.109452, 2023.

Moisseeva, N. and Stull, R.: Wildfire Smoke-Plume Rise: A Simple Energy Balance Parameterization, Atmospheric Chemistry and Physics, 21, 1407–1425, https://doi.org/10.5194/ACP-21-1407-2021, 2021.

Nelson, R. M.: Prediction of Diurnal Change in 10-h Fuel Stick Moisture Content, Canadian Journal of Forest Research, 30, 1071–1087, https://doi.org/10.1139/x00-032, 2000.

Peace, M., Mattner, T., Mills, G., Kepert, J., and McCaw, L.: Fire-Modified Meteorology in a Coupled Fire–Atmosphere Model, Journal of Applied Meteorology and Climatology, 54, 704–720, https://doi.org/10.1175/JAMC-D-14-0063.1, 2015.

Peace, M., Mattner, T., Mills, G., Kepert, J., and McCaw, L.: Coupled Fire–Atmosphere Simulations of the Rocky River Fire Using WRF-SFIRE, Journal of Applied Meteorology and Climatology, 55, 1151–1168, https://doi.org/10.1175/JAMC-D-15-0157.1, 2016.

Potter, B. E.: Atmospheric Interactions with Wildland Fire Behaviour – I. Basic Surface Interactions, Vertical Profiles and Synoptic Structures, International Journal of Wildland Fire, 21, 779–801, https://doi.org/10.1071/WF11128, 2012a.

Potter, B. E.: Atmospheric Interactions with Wildland Fire Behaviour – II. Plume and Vortex Dynamics, International Journal of Wildland Fire, 21, 802–817, https://doi.org/10.1071/WF11129, 2012b.

Ražnjević, A., van Heerwaarden, C., van Stratum, B., Hensen, A., Velzeboer, I., van den Bulk, P., and Krol, M.: Technical Note: Interpretation of Field Observations of Point-Source Methane Plume Using Observation-Driven Large-Eddy Simulations, Atmospheric Chemistry and Physics, 22, 6489–6505, https://doi.org/10.5194/acp-22-6489-2022, 2022.

Ribau, M. C., Bachfischer, M., Miralles, M., Ruiz, B., Stoof, C. R., and de Arellano, J. V.-G.: Pyroconvection Classification Based on Atmospheric Vertical Profiling Correlation with Extreme Fire Spread Observations, Zenodo [Data Set], https://doi.org/10.5281/zenodo.6433389, 2022.

Rio, C., Hourdin, F., and Chédin, A.: Numerical Simulation of Tropospheric Injection of Biomass Burning Products by Pyro-Thermal Plumes, Atmospheric Chemistry and Physics, 10, 3463–3478, https://doi.org/10.5194/acp-10-3463-2010, 2010.

Roberts, M., Lareau, N. P., Juliano, T. W., Shamsaei, K., Ebrahimian, H., and Kosovic, B.: Sensitivity of Simulated Fire-Generated Circulations to Fuel Characteristics During Large Wildfires, Journal of Geophysical Research: Atmospheres, 129, e2023JD040 548, https://doi.org/10.1029/2023JD040548, 2024.

Roelofs, T., Castellnou Ribau, M., Vilà-Guerau De Arellano, J., Janssens, M., and van Heerwaarden, C.: Dataset for Paper: The Impact of the Santa Coloma de Queralt Fire on the Atmospheric Boundary Layer: The Development of a Fire-Induced Circulation [Data Set], https://doi.org/10.5281/zenodo.17159896, 2025.

Sun, R., Jenkins, M. A., Krueger, S. K., Mell, W., and Charney, J. J.: An Evaluation of Fire-Plume Properties Simulated with the Fire Dynamics Simulator (FDS) and the Clark Coupled Wildfire Model, Canadian Journal of Forest Research, 36, 2894–2908, https://doi.org/10.1139/x06-138, 2006.

Sun, R., Krueger, S. K., Jenkins, M. A., Zulauf, M. A., and Charney, J. J.: The Importance of Fire–Atmosphere Coupling and Boundary-Layer Turbulence to Wildfire Spread, International Journal of Wildland Fire, 18, 50–60, https://doi.org/10.1071/WF07072, 2009.

Taszarek, M., Pilguj, N., Allen, J. T., Gensini, V., Brooks, H. E., and Szuster, P.: Comparison of Convective Parameters Derived from ERA5 and MERRA-2 with Rawinsonde Data over Europe and North America, Journal of Climate, 34, 3211–3237, https://doi.org/10.1175/JCLI-D-20-0484.1, 2021.

Tedim, F., Leone, V., Amraoui, M., Bouillon, C., Coughlan, M. R., Delogu, G. M., Fernandes, P. M., Ferreira, C., McCaffrey, S., McGee, T. K., Parente, J., Paton, D., Pereira, M. G., Ribeiro, L. M., Viegas, D. X., and Xanthopoulos, G.: Defining Extreme Wildfire Events: Difficulties, Challenges, and Impacts, Fire, 1, 9, https://doi.org/10.3390/fire1010009, 2018.

van Heerwaarden, C. C., Mellado, J. P., and Lozar, A. D.: Scaling Laws for the Heterogeneously Heated Free Convective Boundary Layer, Journal of the Atmospheric Sciences, 71, 3975–4000, https://doi.org/10.1175/JAS-D-13-0383.1, 2014.

Van Heerwaarden, C. C., Van Stratum, B. J. H., Heus, T., Gibbs, J. A., Fedorovich, E., and Mellado, J. P.: MicroHH 1.0: A Computational Fluid Dynamics Code for Direct Numerical Simulation and Large-Eddy Simulation of Atmospheric Boundary Layer Flows, Geoscientific Model Development, 10, 3145–3165, https://doi.org/10.5194/GMD-10-3145-2017, 2017.

van Stratum, B. J. H., van Heerwaarden, C. C., and Vilà-Guerau de Arellano, J.: The Benefits and Challenges of Downscaling a Global Reanalysis With Doubly-Periodic Large-Eddy Simulations, Journal of Advances in Modeling Earth Systems, 15, https://doi.org/10.1029/2023MS003750, 2023.

Vilà-Guerau De Arellano, J., van Heerwaarden, C. C., Van Stratum, B. J. H., and Van den Dries, K.: Atmospheric Boundary Layer Dynamics, in: ATMOSPHERIC BOUNDARY LAYER: Intergrating Air Chemistry and Land Interactions, pp. 21–32, Cambridge University Press, New York, ISBN 978-1-107-09094-1, 2015.

Werth, P. A., Potter, B. E., Alexander, M. E., Cruz, M. G., Clements, C. B., Finney, M. A., Forthofer, J. M., Goodrick, S. L., Hoffman, C., Jolly, W. M., McAllister, S. S., Ottmar, R. D., and Parsons, R. A.: Synthesis of Knowledge of Extreme Fire Behavior: Volume 2 for Fire Behavior Specialists, Researchers, and Meteorologists, General Technical Report PNW-GTR-891, U.S. Department of Agriculture, Forest Service, Pacific Northwest Research Station, 2016.

Zuo, P., Chen, X., Zhu, L., Zuo, P., Chen, X., and Zhu, L.: Applicability Assessment of ERA5 Surface Wind Speed Data Across Different Landforms in China, Atmosphere, 16, https://doi.org/10.3390/atmos16080956, 2025.